The Astrophysical Journal, 848:103 (26pp), 2017 October 20 https://doi.org/10.3847/1538-4357/aa8ea6

Mrk 421 after the Giant X-Ray Outburst in 2013

B. Kapanadze[1,2], D. Dorner[3], P. Romano[2], S. Vercellone[2], S. Kapanadze[1], and L. Tabagari[1]
[1] E. Kharadze Abastumani Astrophysical Observatory, Ilia State University, Colokashvili Av. 3/5, Tbilisi, 0162, Georgia
[2] INAF, Osservatorio Astronomico di Brera, Via E. Bianchi 46, I-23807 Merate, Italy
[3] Universität Würzburg, Institute for Theoretical Physics and Astrophysics, Emil-Fischer-Str. 31, D-97074 Würtzburg, Germany
Received 2017 July 19; revised 2017 September 9; accepted 2017 September 19; published 2017 October 20

Abstract

We present the results of the *Swift* observations of the nearby BL Lac object Mrk 421 during 2013 November–2015 June. The source exhibited a strong long-term variability in the 0.3–10 keV band, with a maximum-to-minimum flux ratio of 13, and underwent X-ray flares by a factor of 1.8–5.2 on timescales of a few weeks or shorter. The source showed 48 instances of intraday flux variability in this period, which sometimes was observed within the 1 ks observational run. It was characterized by fractional amplitudes of 1.5(0.3)%–38.6(0.4)% and flux doubling/halving times of 2.6–20.1 hr. The X-ray flux showed a lack of correlation with the TeV flux on some occasions (strong TeV flares were not accompanied by comparable X-ray activity and vice versa), indicating that the high-energy emission in Mrk 421 was generated from an emission region more complex than a single zone. The best fits of the 0.3–10 keV spectra were mainly obtained using the log-parabola model, showing a strong spectral variability that generally followed a "harder-when-brighter" trend. The position of the synchrotron spectral energy distribution peak showed an extreme range from a few eV to ∼10 keV that happens rarely in blazars.

Key words: BL Lacertae objects: individual (Mrk 421)

Supporting material: machine-readable tables

1. Introduction

BL Lacertae objects (BLLs) constitute a rare class of active galactic nuclei (AGNs) exhibiting weak or absent emission lines, high and variable radio/optical polarization, superluminal motions, multiwavelength (MWL) flux variability, and a double-humped spectral energy distribution (SED) dominated by nonthermal radiation from the radio to γ-ray frequencies that makes them the most frequently detected class of the extragalactic TeV sources (Falomo et al. 2014). These features are generally attributed to the nonthermal radiation from a relativistic jet closely aligned to our line of sight (Urry & Padovani 1995, and references therein). It is widely accepted that the low-energy SED component is due to the distribution of relativistic electrons radiating via the synchrotron process (Celotti & Ghisellini 2008). Depending on the position of the synchrotron SED peak, BLLs are broadly divided into two subclasses (Padovani & Giommi 1995, and references therein): high-frequency-peaked objects (HBLs, peaking at UV–X-ray frequencies) and low-frequency-peaked objects (LBLs, peaking at infrared–optical frequencies).

There are a variety of models for the origin of the higher-energy bump: an inverse-Compton (IC) scattering of synchrotron photons by their "parent" electron population (so-called synchrotron self-Compton model, SSC; Marscher & Gear 1985) and the hadronic processes (e.g., Mannheim & Biermann 1992). A valid model can be discerned via the intense MWL flux variability and interband cross-correlation study, which also provides important clues about underlying physical processes, the structure, and the dynamics of the BLL emission zone.

In this paper, we present the results related to the X-ray timing and spectral behavior of the nearby HBL source Mrk 421 ($z = 0.031$; Alecsic et al. 2015a) during 2013 November–2015 June, after its giant X-ray outburst in 2013 April (Balocovic et al. 2016; Kapanadze et al. 2016a, hereafter Paper I). First of all, we concentrate on the 0.3–10 keV band observations performed with the X-ray Telescope (XRT; Burrows et al. 2005) on board *Swift* (Gehrels et al. 2004), which allows us to detect a flux variability on timescales from minutes to years, obtain high-quality spectra for the majority of the observations, derive different spectral parameters, and study their timing behavior thanks to its unique characteristics, good photon statistics, and the low background counts. Along with these data, we have analyzed observations performed with the Ultraviolet/Optical Telescope (UVOT; Roming et al. 2005) and the Burst Alert Telescope (BAT; Barthelmy et al. 2005) on board *Swift*. We also constructed light curves using the publicly available TeV (FACT; Anderhub et al. 2013), high-energy (HE, $E > 1$ MeV; Large Area Telescope [LAT] on board *Fermi*; Atwood et al. 2009), optical (R and V bands of Johnson–Cousins system; different Earth-based telescopes), and radio (the Owens Valley Radio Observatory [OVRO] 40 m telescope; Richards et al. 2011) observations for drawing conclusions about the target's MWL behavior and searching for interband correlations. We reconsider the results from Paper I to compare them with those obtained here.

The paper is organized as follows. Section 2 describes the data processing and analyzing procedures. In Sections 3–4, we provide the results of a timing and spectral analysis. We discuss our results in Section 5 and provide our conclusions in Section 6.

2. Observations and Data Reduction

2.1. X-Ray Data

The Level 1 unscreened XRT event files were processed with the `XRTDAS` package developed at the ASI Science Data Center (ASDC) and distributed by HEASARC within the `HEASOFT` package (v.6.20). They were reduced, calibrated, and cleaned by means of the `XRTPIPELINE` script using the standard filtering criteria and the latest calibration files of *Swift*

CALDB v.20160731. We selected the events with the 0–2 grades for the Windowed Timing (WT) mode, used to observe Mrk 421.

The source and background light curves and spectra were extracted with XSELECT using the circular area with radii of 30–60 pixels depending on the source brightness and exposure. For the count rates $\sim$100 counts s^{-1} and higher, a pileup correction was performed according to the recipe provided in Romano et al. (2006). The light curves were then corrected using XRTLCCORR for the resultant loss of effective area, bad/hot pixels, pileup, and vignetting. The ancillary response files (ARFs) were generated using the XRTMKARF task, with the corrections on the point-spread function losses, different extraction regions, vignetting, and CCD defects. The instrumental channels were combined using GRPPHA to include at least 20 photons per bin.

From the daily binned BAT data, obtained within the *Swift*-BAT Hard X-ray Transient Monitor program[4] (Krimm et al. 2013), we used only those corresponding to the detection of the source with 5σ significance (the threshold generally accepted for coded-mask devices) to study a variability of the 15–150 keV flux. However, we also plotted the data corresponding to the detection with $3\,\sigma$ significance in Figure 1(c), used by some authors for a flux variability study (see, e.g., Horan et al. 2009). From the publicly available weekly and daily binned 2–20 keV data, obtained with *MAXI*[5] (Matsuoka et al. 2009), we used only those corresponding to the aforementioned significance.

2.2. γ-ray Data

We extracted the 0.3–300 GeV fluxes from the LAT observations using the events of the diffuse class from a region of interest (ROI) of radius 10°, centered on Mrk 421 and processed with the *Fermi* Science Tools package (version v10r0p5) and P8R2_V6 instrument response function using an unbinned maximum likelihood method GTLIKE. A cut on the zenith angle (>100°) was applied to reduce contamination from the Earth-albedo γ-rays. The data taken when the rocking angle of the spacecraft is larger than 52° are discarded to avoid contamination from photons from the Earth's limb. A background model including all γ-ray sources from the *Fermi*-LAT 4 yr Point Source Catalog (3FGL; Acero et al. 2015) within 20° of Mrk 421 was created. The spectral parameters of sources within the ROI are left free during the minimization process, while those outside of this range were held fixed to the 3FGL catalog values. The Galactic and extragalactic diffuse γ-ray emission and the residual instrumental background are included using the recommended model files gll_iem_v06.fits and iso_P8R2_SOURCE_V6_v06.txt. The normalizations of both components in the background model were allowed to vary freely during the spectral fitting. For the spectral modeling of Mrk 421, we adopted a simple power law, as done in the 3FGL catalog.

Mrk 421 is one of the sources regularly monitored by the First G-APD Cherenkov Telescope (FACT) at TeV energies. This imaging air Cerenkov telescope is located in the Observatorio del Roque de los Muchachos (La Palma, Spain) and has been operational since 2011 October. Since 2012 December, the FACT collaboration has published the results of a preliminary quick-look analysis with a low latency online.[6] Applying no data quality selection, the quick-look analysis provides background-subtracted light curves that are not corrected for the effect of changing energy threshold, which changes with changing zenith distance and different ambient light conditions. The analysis is described in detail in Dorner et al. (2015). In total, about 1290 hr of data are available from FACT between 2012 December and 2016 June. For our study, we restricted the sample to nights having a signal detected with at least 3σ significance, resulting in 89 nights (267.2 hr) for the study between 2013 November and 2015 May and 186 nights (581.6 hr) in total. From the total data sample, 83.5% have been taken with ambient light and zenith distance conditions in which the energy threshold does not change significantly. The nightly observation time is between 0.3 and 7.5 hr.

2.3. UV, Optical, and Radio Data

The photometry for the sky-corrected images obtained in the UVOT bands UVW1, UVM2, and UVW2 was performed using the UVOTSOURCE tool (developed and distributed within HEASOFT), and the calibration files were included in the CALDB. By means of this tool, we performed a correction for coincidence losses, applied background subtraction, and calculated the target's magnitude and the associated error. The measurements were done using a circular source region of the 20 arcsec radius, since the source was very bright in these bands. In the case of magnitudes smaller than 12 mag, a pileup was estimated and the corresponding correction was performed using the recipe provided in Page et al. (2013). The magnitudes were then corrected for the Galactic absorption by applying $E(B-V) = 0.028$ mag (Paper I) and the $A_\lambda/E(B-V)$ values derived from the interstellar extinction curves (Fitzpartick & Messa 2007), using the effective wavelength of each filter from Poole (2008). We converted them into linear fluxes (in mJy) by adopting the latest photometric zero-points for each band provided in Breeveld et al. (2011), and then we subtracted 0.09, 0.05, and 0.06 mJy for the UVW1, UVM2, and UVW2 bands, respectively, to remove the host contribution (see Paper I).

We extracted the publicly available *V*- and *R*-band (Johnson–Cousins system) data obtained with the 2.3 m Bock and 1.54 m Kuiper telescopes of Steward observatory[7] (see Smith et al. 2009, for details). We have dereddened and converted the corresponding magnitudes into linear fluxes according to Bessel (1979). In the *R* band, the host contribution is subtracted from the total flux according to Nilsson et al. (2007). The host contribution in the *V* band was derived according to Fukugita et al. (1995) and subtracted from the total *V*-band flux.

Regular 15 GHz observations of Mrk 421 were performed with the 40 m telescope of OVRO (Richards et al. 2011). We retrieved the publicly available OVRO data of our target from the corresponding website.[8] The details of the data reduction and calibration procedure can be found in Richards et al.

Throughout this paper, the errors are quoted at the 90% confidence level for the one parameter of interest $\Delta_{\chi^2} = 2.71$, unless otherwise stated.

[4] http://swift.gsfc.nasa.gov/results/transients/weak/Mrk421/
[5] http://maxi.riken.jp/
[6] http://www.fact-project.org/monitoring
[7] See http://james.as.arizona.edu/~spsmith/Fermi/.
[8] See http://www.astro.caltech.edu/ovroblazars/.

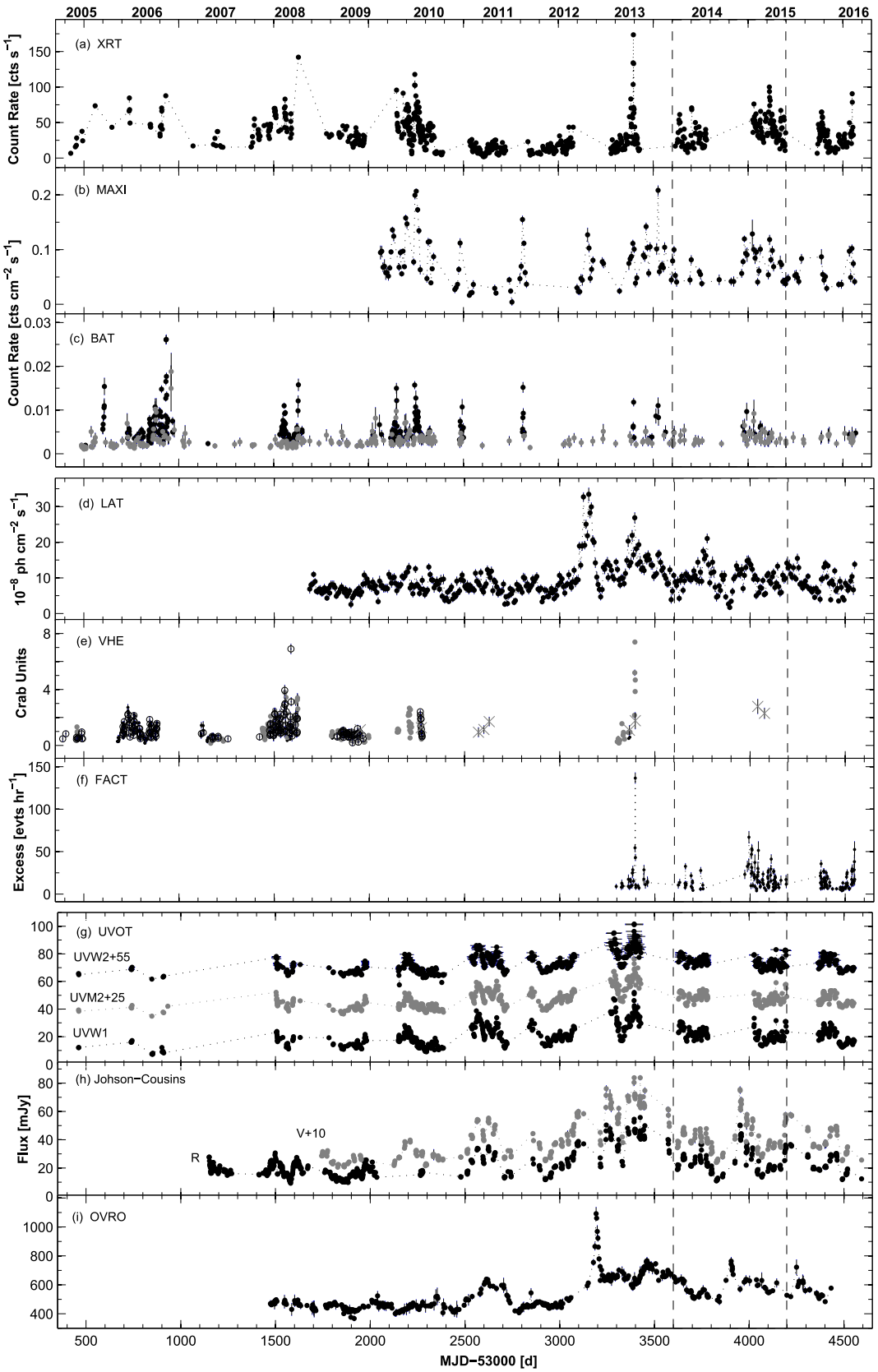

Figure 1. Historical light curves of Mrk 421 from the MWL observations in 2005–2016 performed with (a) XRT, (b) *MAXI*, (c) BAT (black and gray points stand for the detections with 5σ and 3σ significance, respectively), (d) LAT, (e) VHE (black points correspond to the VERITAS data; gray points, open circles, and asterisks correspond to those from the MAGIC, Whipple, and HAGAR observations, respectively), (f) FACT, (g) UVOT, (h) ground-based optical telescopes, and (i) the OVRO 40 m telescope. We used daily bins for XRT, BAT, FACT, UVOT, Steward, and OVRO data and 1-week bins for those of *MAXI* of LAT observations. The period 2013 November–2015 June (MJD 56,600–57,200) is confined within vertical dashed lines.

Table 1
Summary of the XRT and UVOT Observations in 2013 November–2015 June

ObsID	Obs. Start–End (UTC)	Exp. (s)	MJD	CR (counts s^{-1})	UVW1 (mag)	UVW1 (mJy)	UVM2 (mag)	UVM2 (mJy)	UVW2 (mag)	UVW2 (mJy)
(1)	(2)	(3)	(4)	(5)	(6)	(7)	(8)	(9)	(10)	(11)
31202141	2013 Nov 20 18:46:47 20:29:32	996	56,616.786	16.64(0.14)	...	...	...	...	...	...
31202142	Nov 20 19:09:12 21:08:45	996	56,616.799	17.64(0.10)	...	...	...	...	...	...
35014077	Dec 01 06:14:58 07:21:19	1104	56,627.262	22.19(0.15)	11.48(0.11)	22.82(0.71)	11.62(0.10)	17.17(0.25)	11.47(0.10)	18.99(0.45)
35014078	Dec 03 12:41:00 13:47:48	1169	56,629.530	25.25(0.16)	11.45(0.11)	23.46(0.71)	11.57(0.10)	17.98(0.25)	11.44(0.10)	19.53(0.45)

Note. The columns are as follows: (1) observation ID; (2) observation start and end (in UTC); (3) exposure (in seconds); (4) modified Julian date of the observation start; (5) observation-binned count rate with its error; (6)–(11) dereddened UVOT magnitudes and corresponding fluxes.

(This table is available in its entirety in machine-readable form.)

3. Results from the MWL Temporal Study

3.1. Long-term X-Ray Variability

The source was observed 161 times by XRT between 2013 November 20 and 2015 June 24 with a total exposure of 172.8 ks, including our Target of Opportunity observations. The information about each pointing and the corresponding count rates are provided in Table 1.[9] The same table also contains the results of the UVOT observations (dereddened magnitudes and corresponding fluxes in each band).

The historical light curve of Mrk 421 from XRT observations (Figure 1(a)) shows that the whole 2013 November 20–2015 June 24 period can be divided into two parts characterized by the intense XRT monitoring ("Period 2": 2013 November–2014 May; "Period 3": 2015 January–June) and separated by the almost 8-month break in the observations. Although the source showed a strong X-ray variability in both periods with the 0.3–10 keV count rate ranging between 7.66 ± 0.12 counts s^{-1} and 99.90 ± 0.32 counts s^{-1}, it was less extreme than that in 2013 April (hereafter "Period 1," comprising also the time interval between the giant outburst and mid-May 2013, until the stop in the *Swift* observations of our target), when the 0.3–10 keV count rate attained a value of 260.71 ± 2.79 counts s^{-1} (1-minute binning; Paper I).

Figures 2(Ba)–(Ca) show that the source underwent several shorter-term X-ray flares by a factor of 1.8–5.2 on timescales of a few weeks in Periods 2–3 (see Section 3.4 for details). Note that, on average, the source was brighter in Period 3 than in the previous period (with the weighted mean 0.3–10 keV count rates of 36.58 ± 0.03 counts s^{-1} and 25.32 ± 0.02 counts s^{-1}, respectively). Although the source was not as strongly variable in 2013 November–2015 June as in Period 1 and did not show giant outbursts, Mrk 421 was the brightest and the most violently variable blazar in X-rays also during this period.

In Period 3, the source showed a larger variability (maximum-to-minimum flux ratio $R = 3.2$ vs. $R = 2.2$ in Period 2), and it was detected more frequently from 1-week binned *MAXI* data (18 detections with 5σ significance in 186 days; only 7 detections in 175 days in the previous period) than in Period 2 (Figures 2(Bb)–(Cb)). The corresponding light curve exhibits its peaks in the epochs of the 0.3–10 keV flares. For the whole 2013 November–2015 June period, the ratio $R = 3.4$, which is much smaller compared to the same ratio in the XRT band ($R = 13$) that can be related to the significantly lower instrumental characteristics of *MAXI*. On average, the source was brighter in the 2–20 keV band in Period 1 and during the strong flaring activity in 2010 (Figure 1(b)).

The source was detected 5 times at the 5σ confidence level in Period 3 with $R = 2.1$, while it was detected only with 3σ significance in Period 2 from the daily binned BAT data (Figure 1(c)). In this band, the source showed stronger activity in previous years, and a very strong 15–150 keV flare by a factor of 7 was observed in 2006 April–July (composing 41% of all detections with 5σ).

3.2. Long-term γ-ray Variability

The source generally was detectable with the 2-day binned LAT data in both periods (except for three and one cases in Periods 2 and 3, respectively; Figures 2(Bc)–(Cc)). Note that Period 2 was remarkable for the higher weighted mean 0.3–300 GeV photon flux than in the next period (9.55 vs. 7.25, in units of 10^{-8} photons cm^{-2} s^{-1}) and the corresponding maximum flux ($(3.19 \pm 0.35) \times 10^{-7}$ photons cm^{-2} s^{-1}) was 12% higher than that from the epoch of a giant X-ray flare in 2013 April (see Figure 2(Ac)). During the 8-month interval between Periods 2 and 3, the source showed lower flux values, and it was relatively often detectable below the 3σ significance with the 2-day binned data, or showed small values of the parameter $N_{\rm pred}$ (the predicted photon count) and, therefore, less credible results. On the other hand, the source showed higher 0.3–300 GeV fluxes during the days just preceding Period 1, and a strong, prolonged HE flare by a factor of 10 was observed in 2012 (Figure 1(d)).

Figure 1(e) present a historical very high-energy (VHE; $E > 100$ GeV) light curve of Mrk 421 (in Crab units), constructed using the data of VERITAS (collected from the VERITAS website;[10] Alecsic et al. 2015a, 2015b; Balocovic et al. 2016), MAGIC (Steinke 2012; Preziuso 2013; Alecsic et al. 2015a, 2015b; Ahnen et al. 2016), Whipple (Acciari et al. 2014), and HAGAR (Sinha et al. 2016). The VHE flux (in units of photons cm^{-2} s^{-1}) was converted into Crab units using the relations 1 Crab $= 1.96 \times 10^{-10}$ photons cm^{-2} s^{-1} for the data with $E > 200$ GeV (Albert et al. 2008) and 1 Crab $= 8.08 \times 10^{-11}$ photons cm^{-2} s^{-1} for those with $E > 400$ GeV (Ahnen

[9] The three leading zeros in observation IDs are omitted everywhere in the paper.

[10] http://veritas.sao.arizona.edu/veritas-science/veritas-blazar-spectra

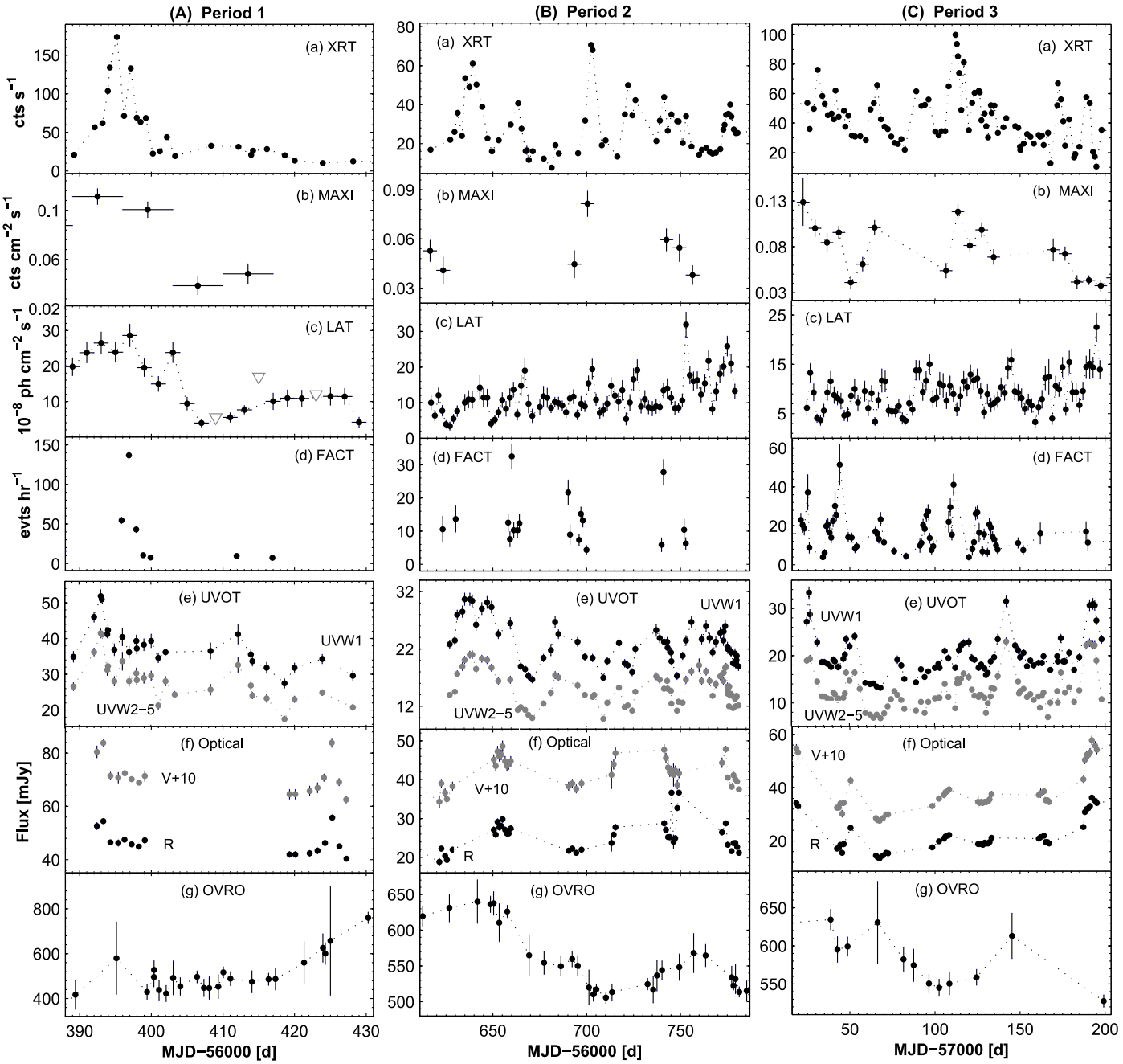

Figure 2. MWL light curves of Mrk 421 in different periods (with the same time bins, except for the LAT data binned within 2-day intervals).

et al. 2016). During 2005–2015, the source showed an overall variability by a factor of about 39 and underwent strong VHE flares in 2008 and Period 1.

The source was detected 88 times with 3σ significance from the 1-day binned FACT data during 2013 November–2015 June (amounting to 47% of all detections between 2012 December and 2016 June). Although the source showed a strong VHE variability with $R = 13.1$ and underwent several short-term flares by a factor of 2.6–13 (lasting from several days to a few weeks), the maximum daily binned VHE excess from this period was a factor of 2.7 smaller than that in the epoch of a giant X-ray flare in Period 1 (see Figures 1(f) and 2(Ad)–(Cd)).

3.3. Long-term Variability in Other Spectral Bands

The source showed a much weaker and slower variability with $R = 2.02$–2.51 in the UVW1–UVW2 bands than in the X-ray-TeV energy range (Figures 2(Be)–(Ce)), and the peaks of the UV light curves mainly did not coincide with those in the 0.3–10 keV band. Sometimes, the source did not exhibit an increasing UV activity and even showed a decline or a minimum along with strong X-ray flares (see Section 3.4 for details). Note that the source often exhibited higher UV states in previous years, especially in the first half of 2013 when the highest UVW1–UVW2 fluxes were observed in the epoch of the giant X-ray outburst (Figure 1(g)). We observe a similar behavior in the optical bands (Figure 2(Bf)–(Cf)), where the

variability was larger with $R = 3.9$–4.8. This result is mainly related to the strong optical flare during MJD 56,827–56,953, when the source was not observed by UVOT. The source showed its highest optical states in 2013 April (similar to the 0.3–10 keV, 0.3–300 GeV, and VHE bands), and, on average, it was significantly brighter during 2011–2016 than in previous years (Figure 1(h)).

Mrk 421 showed the weakest and the slowest variability in the radio band: the 15 GHz showed an overall variability with $R = 1.26$, which was especially weak in Period 3 (possibly related to very sparse observations in this period; Figures 2(Bg)–(Cg)). Note that the source showed a higher radio state at the end of Period 1 (Figure 2(Ag)), and the highest historical 15 GHz flux was observed during the relatively strong and fast flare by a factor of 1.84 in 47 days in 2012, exceeding the threshold of 1 Jy (which is uncommon for HBLs at radio frequencies; Figure 1(i)).

3.4. Shorter-term Flares

Below, we concentrate on the results from the different subperiods (based on the occurrence of short-term flares in the XRT band), whose summary is presented in Table 2. For each flare, the fractional variability amplitude was calculated as (Vaughan et al. 2003)

$$F_{\rm var} = 100((S^2 - \overline{\sigma_{\rm err}^2})/\overline{F})^{1/2}\ \%, \quad (1)$$

with S^2 is the sample variance, $\overline{\sigma_{\rm err}^2}$ is the mean square error, $\overline{F}$ is the mean flux. The MWL light curves from each subperiod are presented in Figure 3.

3.4.1. Period 2

The source showed two subsequent 0.3–10 keV flares by a factor of 2.5–3.6 in 13–22 days in Period 2a (see Table 2 and Figure 3(a)), and the second one was accompanied by a fast TeV flare by a factor of 2.6 in 2 days in the FACT band (no FACT observations were performed along with the first X-ray flare). Although we observe enhanced HE activity along with the onset of both X-ray flares, the corresponding 0.3–300 GeV peaks showed a delay by 4 days with respect to X-ray ones. We observe a UV brightening along with the first X-ray flare, but the source exhibited a decline in the epoch of the second flare. Similarly, the UVW2-band light curve showed a decline in Period 2b when the source showed simultaneous flaring activity in the XRT and LAT bands (by a factor of 4.7 and 2.9, respectively; Figure 3(b)). No firm conclusion can be draw about the VHE activity in the epoch of the X-ray peak, due to missing FACT observations, although we observe a decline in the VHE excess rates during MJD 56,697–56,700, while the X-ray brightness showed an increase.

Short-term X-ray flares by a factor of 2.1–3.7 were accompanied by an enhanced HE activity in Period 2c (Figure 3(c)). However, we observe only an increase by 60% in the 0.3–300 GeV flux around MJD 56,741 (corresponding to the second X-ray peak, accompanied by a fast VHE flare by a factor of 4.7). In contrast, the source underwent an HE flare by a factor of 3.7 and attained its highest state in the here-presented 1.6 yr period during MJD 56,751–56,753, while it brightened only by 70% in the XRT band. Moreover, this period was also characterized by uncorrelated UV–X-ray variability: the UVW2-band light curve exhibits its minimum in the epoch of the first XRT-band peak and a decline along with the second X-ray flare. The source was observed only during MJD 56,740–56,755 by FACT, and it underwent a fast VHE flare by a factor of 5, with a peak coinciding with that in the 0.3–10 keV band on MJD 56,741. However, we observe a low VHE state around MJD 56,753, when Mrk 421 exhibited an X-ray brightening by 70%.

Mrk 421 showed its first HE peak in the epoch of the 0.3–10 keV flare by a factor of 2.6 in Period 2d, but the first one was observed at about MJD 56,765, when the source did not vary significantly in X-rays (Figure 3(d)). During this subperiod, the UV and optical light curves showed a longer-term decreasing trend, with some low-amplitude flux enhancement along with the second HE flare.

3.4.2. Period 3

In the first half of Period 3a (see Table 2), an X-ray flare by a factor of 2.1 coincided with low HE and UV states (Figure 3(e)). However, we cannot draw a firm conclusion on whether this flare was an "orphan" since there was a break in the FACT observations during MJD 57,026–57,034. Afterward, the source showed a very strong VHE flare by a factor of 13.2, and the source reached its highest FACT-band excess rate in the period 2013 November–2015 June on MJD 57,044. Along with this event, the source showed a HE flare by a factor of 3.2. Although the source was keeping its high X-ray brightness level (the 0.3–10 keV count rate showed minor fluctuations around the level of 45 counts s^{-1}, which is 35% higher than the weighted mean rate during 2005–2015) and showed a fast increase by 45% in $\sim$1 day (on MJD 57,042), no comparable activity was observed in the FACT and LAT bands.

An X-ray flare by a factor of 2.1 was followed by enhanced activities in the VHE and HE bands with some time shift in Period 3b (Figure 3(f)). A similar situation was seen in the first half of Period 3c, when the 2.8-fold increase in the 0.3–10 keV flare was accompanied by higher-energy flares by a factor of 3.9 and 6.2 in the LAT and FACT bands, respectively, with a tighter correlation between the X-ray and HE variabilities (Figure 3(g)). However, the next X-ray flare by a factor of 2.9 with the highest 0.3–10 keV state in 2013 November–2015 June (on MJD 57,112) was accompanied by comparable activity only in the VHE band. We observe almost the opposite behavior in the UVW2 band with respect to the X-ray one during both subperiods.

Period 3d (see Table 2) was characterized by a long-term brightness decrease, superimposed by the four consecutive, low-amplitude (by 30%–75%) flux increase and decline cycles, each lasting 6–21 days (Figure 3(h)). During the first two events, the source was detected frequently by FACT, and the corresponding light curve followed the X-ray one closely, exhibiting VHE flares by a factor of 3.2–6.9. In the epoch of the third X-ray cycle, we observe the LAT and UVW2-band flares by a factor of 2.2–2.4 (with a highest UV brightness during the here-presented 1.6 yr period; MJD $\sim$ 57,142). Note that the source showed another HE flare by a factor of 3.9 at the end of this subperiod, while we do not observe comparable activity in the 0.3–10 keV and UVW2 bands.

Finally, the source underwent a strong X-ray flare by a factor of 5.2 in 4 days, accompanied by the 3.6-fold increase in the 0.3–300 GeV flux at the start of Period 3e (see Figure 3(i)). The declining phase of this flare was superimposed by a 72% increase in the 0.3–10 keV flux (peaking on MJD 57,179), and the simultaneous HE flare by a factor of 2.6 was also seen.

Table 2
Summary of the XRT, UVOT, OVRO, *MAXI*, LAT, and FACT Observations in Different Periods

		XRT							UVOT			Optical		OVRO	LAT	FACT
Per. (1)	Dates (2)	$CR_{\max}$ (3)	R (4)	$F_{\rm var}$ (5)	$F_{2-10}^{\max}$ (6)	R_{2-10} (7)	$F_{0.3-2}^{\max}$ (8)	$R_{0.3-2}$ (9)	$R_{\rm W2}$ (10)	$R_{\rm M2}$ (11)	$R_{\rm W1}$ (12)	$R_{\rm V}$ (13)	$R_{\rm R}$ (14)	R (15)	R (16)	R (17)
1	2013-04-07 to 2013-05-16	173.6	16.97	83.4(0.1)	392.64	79.97	313.33	13.52	2.13	1.85	1.89	1.41	1.36	1.14	7.31	18.24
1a	2013-04-07 to 2013-04-18	173.6	8.98	66.0(0.1)	392.64	30.97	313.33	8.43	1.84	1.71	1.5	1.16	1.21	1.07	3.06	18.24
1b	2013-04-18 to 2013-05-16	32.61	3.19	36.3(0.3)	26.12	5.32	68.71	2.96	1.68	1.58	1.50	1.41	1.36	1.13	2.92	1.70
2	2013-11-20 to 2014-05-03	70.64	9.22	44.2(0.1)	99.31	22.73	157.4	7.98	1.74	1.96	1.84	1.59	1.99	1.27	9.26	7.50
2a	2013-11-20 to 2014-01-24	61.17	7.99	51.1(4.4)	99.31	22.73	110.4	5.60	1.74	1.86	1.84	1.59	1.55	1.15	5.52	4.31
2b	2014-01-24 to 2014-02-28	70.64	9.22	81.1(0.2)	84.53	19.34	157.4	7.98	1.52	1.57	1.57	1.33	1.26	1.10	2.94	4.99
2c	2014-02-28 to 2014-04-12	50.04	3.74	34.4(0.2)	57.28	7.38	99.80	3.87	1.49	1.47	1.54	1.32	1.53	1.10	5.89	4.36
2d	2014-04-12 to 2014-05-03	40.11	2.8	33.2(0.2)	52.60	5.02	99.10	3.54	1.43	1.39	1.37	1.37	1.36	1.10	3.16	...
3	2015-01-01 to 2015-06-24	99.90	9.49	40.8(0.1)	140.93	27.80	166.70	7.31	2.38	2.69	2.58	2.57	2.69	1.20	6.9	13.17
3a	2015-01-01 to 2015-02-06	76.11	2.68	26.9(0.1)	112.98	4.95	129.40	4.19	1.56	1.93	2.34	1.62	1.60	1.07	3.62	13.16
3b	2015-02-06 to 2015-03-01	65.74	3.02	35.4(0.3)	106.17	7.05	123.30	3.98	1.82	1.54	1.45	1.13	1.19	1.08	3.51	5.31
3c	2015-03-01 to 2015-04-07	99.90	4.58	41.8(0.1)	140.93	9.35	166.70	5.38	1.65	1.65	1.59	1.27	1.26	1.05	4.21	10.49
3d	2015-04-07 to 2015-05-25	61.86	4.84	32.8(0.2)	86.10	4.59	131.2	3.36	2.17	2.15	1.98	1.94	1.22	1.10	4.87	6.86
3e	2015-04-07 to 2015-05-25	66.98	7.06	53.7(0.2)	68.71	13.55	119.4	5.24	1.84	1.89	1.82	1.44	1.44	1.00	5.62	1.49

Note. Columns (3)–(5): maximum 0.3–10 keV flux (in counts s^{-1}), maximum-to-minimum flux ratio, and fractional amplitude in each period, respectively. Columns (6)–(9): maximum values (in 10^{-11} erg cm^{-2} s^{-1}) and maximum-to-minimum flux ratios for unabsorbed 0.3–2 keV and 2–10 keV fluxes. Columns (10)–(14): maximum-to-minimum flux ratios in the UVOT UVW1–UVW2 and optical *V*–*R* bands. Columns (15)–(17): maximum-to-minimum flux ratios from the LAT and FACT observations.

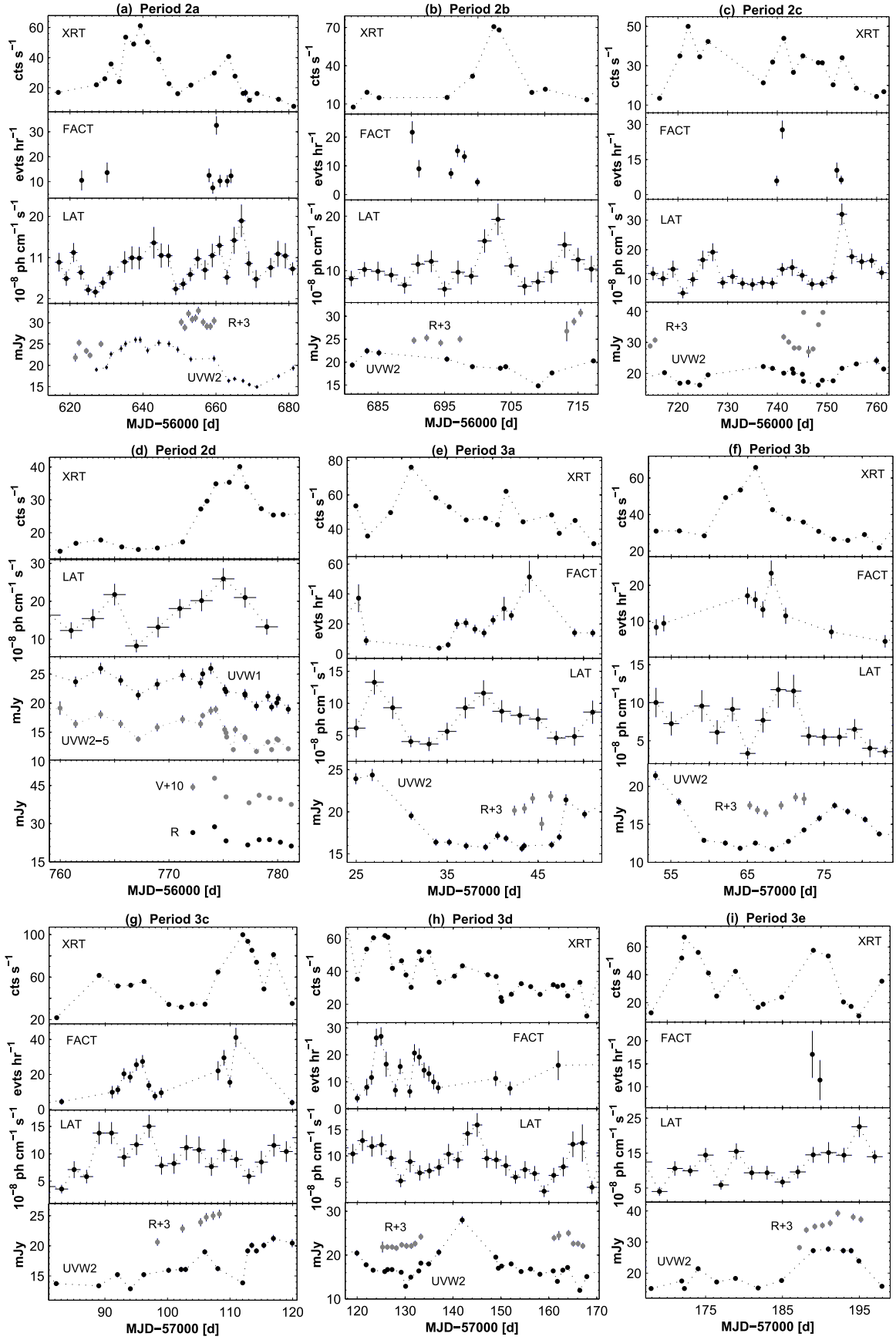

Figure 3. Multiwavelength variability of Mrk 421 in subperiods. Daily bins are used for the XRT, FACT, UVOT, Steward, and OVRO light curves, and 2-day bins are used for the LAT data.

Although the second X-ray flare by a factor of 3.5 during MJD 57,182–57,189 was followed by UV and HE brightenings, a higher 0.3–300 GeV state was then superimposed by the subsequent brightness increase by 57%, whose peak coincided with the minimum in the XRT-band light curve (on MJD 57,195). The source was observed by FACT during the aforementioned short-term X-ray brightening and during the second X-ray flare, but it was detected only twice with 3σ significance, and the corresponding excess rates do not correspond to a higher VHE state.

3.5. Intraday Variability

We detected 48 XRT instances of the intraday 0.3–10 keV variability (IDV), defined as a flux change with 99.9% confidence within a day (the threshold generally used for this purpose; see, e.g., Andruchow et al. 2005) using the χ^2-statistics. For each event, the values of reduced χ^2, fractional variability amplitude, and the ranges of the spectral parameters a, b, $E_{\rm p}$, and HR (derived from the separate orbits of the corresponding observation with the log-parabolic or power-law spectral models; see Section 4 for their definitions) are provided along with each event.

Figure 4 presents the most extreme IDVs, which were observed in Periods 2–3. The fastest variability was recorded on 2015 June 7, when the 0.3–10 keV flux increased and declined by ∼7% in 0.45 ks (Figure 4(a)). The source showed two consecutive fluctuations by ∼8% within 1 ks on 2015 April 28 (Figure 4(b)). The X-ray brightness increased by 12% in 0.3 ks and then declined by 5% in 0.18 ks on 2015 April 4 (Figure 4(c)). A similar behavior was observed on 2015 January 11 (an increase by 9% and subsequent decline by 5% within 0.6 ks; Figure 4(d)). In the same time, the source brightened by 7% on 2015 January 13 (Figure 4(e)) and showed a decline by 10%–20% in 0.6–1.08 ks on 2015 May 29, 2013 December 13 and 23, and 2014 February 11 (Figures 4(f)–(i)).

The largest IDVs were recorded on 2014 April 30, when the brightness dropped by a factor of ∼2.2 in about 10.5 ks (between the second orbit of ObsID 35014120 and the first orbit of ObsID 35014120; Figure 4(j)). Afterward, it increased by 80% in about 3.5 ks, followed by a decline by 30% in 4.5 ks. The 0.3–10 keV flux doubled between the two short XRT observations separated by about 20.2 hr from each other on 2014 May 2 (ObsIDs 35014149 and 35014150, each lasting 0.43–0.52 ks; MJD 56,779). The source also showed a strong IDV on 2014 March 27, when the flux almost halved in 10.5 ks (a decline by 45%; between the first and third orbits of MJD 35,014,120; Figure 4(k)) and then increased by 36% in 4 ks.

However, the source sometimes varied very slowly on intraday timescales, as revealed from the densely sampled XRT observations. For example, the 0.3–10 keV flux increased only by 24% during 74.5 ks on 2014 April 28/29 (Figure 5(a)). Even slower variability was recorded during 2015 March 31—April 3 (containing the moment of the highest X-ray brightness during 2013 November–2015 June): the brightness decreased only by 32% in 2.28 days, and it halved in 3.4 days.

We have found the eight 0.3–10 keV IDVs with 99.5% significance (so-called possible variability; Andruchow et al. 2005), whose summary is also given in Table 3. Figures 6(a)–(d) present the most extreme four cases with a brightness increase or decline by 9%–19% within 0.54–0.96 s and fractional amplitudes $F_{\rm var} = 2.2\%$–2.6%.

Figure 6(e) presents the VHE light curves constructed using the 20-minute binned FACT data from the most active nights. In contrast to Period 1a (see Paper I), the source did not show a VHE IDV during any night.

Figure 6(f) presents the 0.3–300 GeV light curve from the period 2014 April 24–May 1, when the source was most active in this band and the source was detectable with 3σ significance from 0.5-day bins. The flux showed an increase by a factor of 3.15 in 3 days, and then it dropped by a factor of 2.7 within 1 day (during MJD 56,774.5–56,775.5). Note that the UVOT flux also showed a decline by ∼70% along with the HE one, and the four other IDVs with $F_{\rm var} = 4.3(0.7)\%$–$12.6(0.8)\%$ occurred during the next days (Figure 6(g)). The source showed the UVOT-band IDVs on MJD 57,129 and MJD 57,133 (Figure 6(h); $F_{\rm var} = 13.0(1.2)\%$–$15.2(1.6)\%$), as well as during MJD 57,047.33–57,048.07, with an increase of 11%–34% in the UV flux (with larger variability toward increasing frequencies; Figure 6(i)).

4. Spectral Results

4.1. Spectral Curvature

We performed the 0.3–10 keV spectral analysis by fixing the hydrogen column density to the Galactic value $N_{\rm H} = 1.90 \times 10^{20}$ cm^{-2} (Kalberla et al. 2005) and using the log-parabolic model (LP; Massaro et al. 2004, hereafter M04)

$$F(E) = K(E/E_1)^{-(a+b\log(E/E_1))}, \quad (2)$$

where $E_1 = 1$ keV, a is the photon index at the energy E_1, b is the curvature parameter, and K is the normalization factor. The position of the SED peak and its height are given by

$$E_{\rm p} = E_1 10^{(2-a)/2b} \text{ keV}, \quad (3)$$

$$S_{\rm p} = 1.6 \times 10^{-9} K 10^{(2-a)^2/4b)} \text{ erg cm}^{-2}\text{ s}^{-1}. \quad (4)$$

We extracted the spectra from separate orbits of a single observation when it was impossible to use the same source and background extraction regions for all orbits, or the source showed a flux variability during this observation. We used the same method even for a single orbit, when the flux varied within it, or there was no satisfactory value of the reduced chi-square for the spectrum extracted from the whole orbit (although the presence of a spectral curvature was evident). In similar situations, we extracted the spectra even from the segments of the particular orbit. For each spectrum, the model validity was checked by means of reduced chi-squared, the distribution of the residuals, and an F-test. We calculated unabsorbed 0.3–2 keV, 2–10 keV, and 0.3–10 keV fluxes using the `EDITMOD` task. The hardness ratio (HR) is calculated as a ratio of unabsorbed 2–10 keV to 0.3–2 keV fluxes.

For the majority of the 0.3–10 keV spectra of Mrk 421 in 2013 November–2015 June, a simple power law (PL) $F(E) = KE^{-\Gamma}$ (where Γ is the photon index throughout the observation band and K is the normalization factor) was excluded at the 99.99% confidence level, and the LP model was clearly preferred by the aforementioned tests (for 540 out of 568 spectra; see Table 4 for the corresponding results). In Table 5, we present the properties of the distribution of the a, HR, and b parameters for the whole 2013 November–2015 June period, as well as for Periods 1a, 2, and 3 separately. We chose the spectral data from Period 1a (i.e., the epoch of the giant outburst) for a comparison to those from Periods 2–3. In Period 1b, the source was less variable in the 0.3–10 keV band

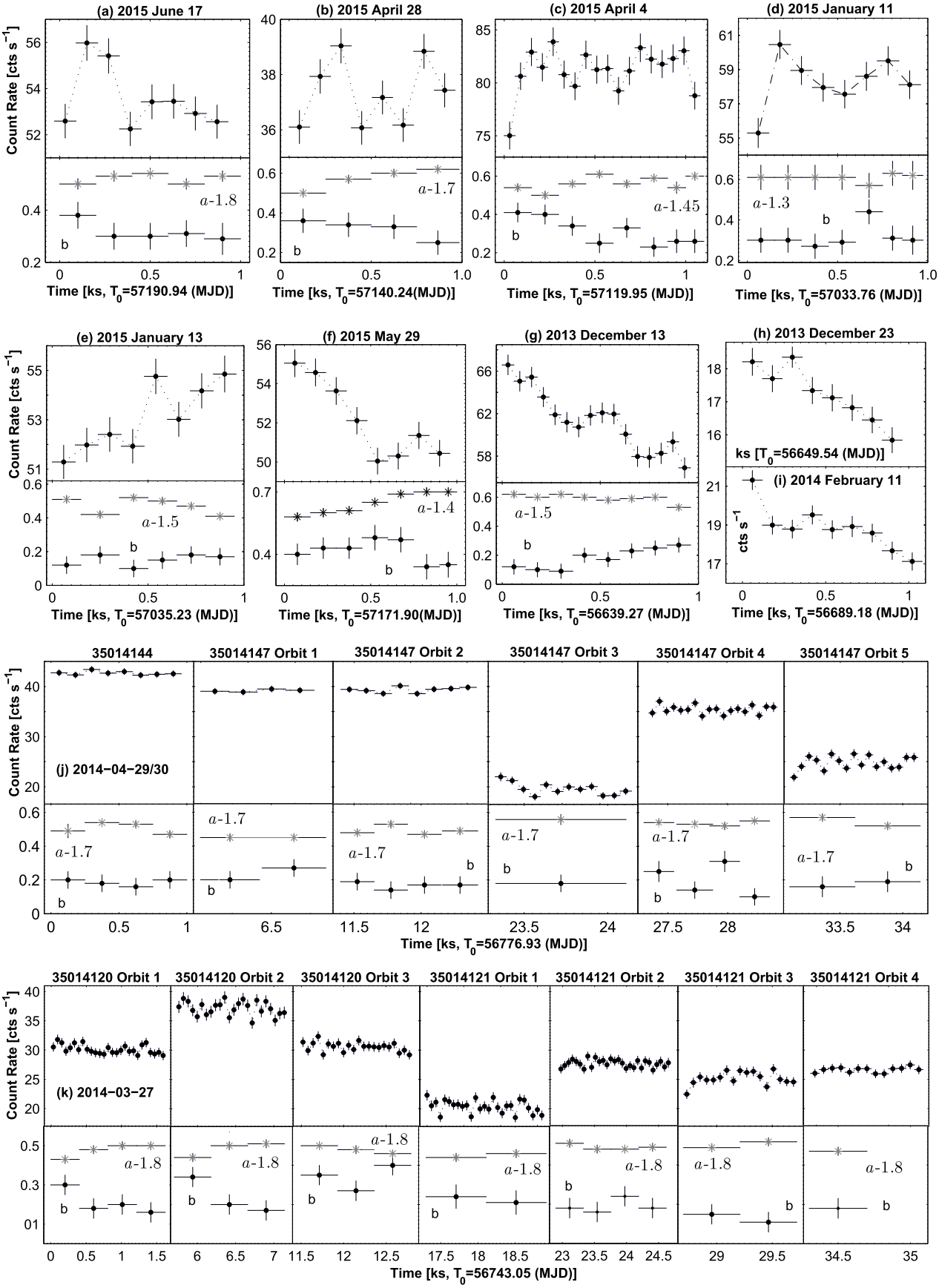

Figure 4. Most remarkable 0.3–10 keV IDVs in 2013 November–2015 June detected with 99.9% confidence.

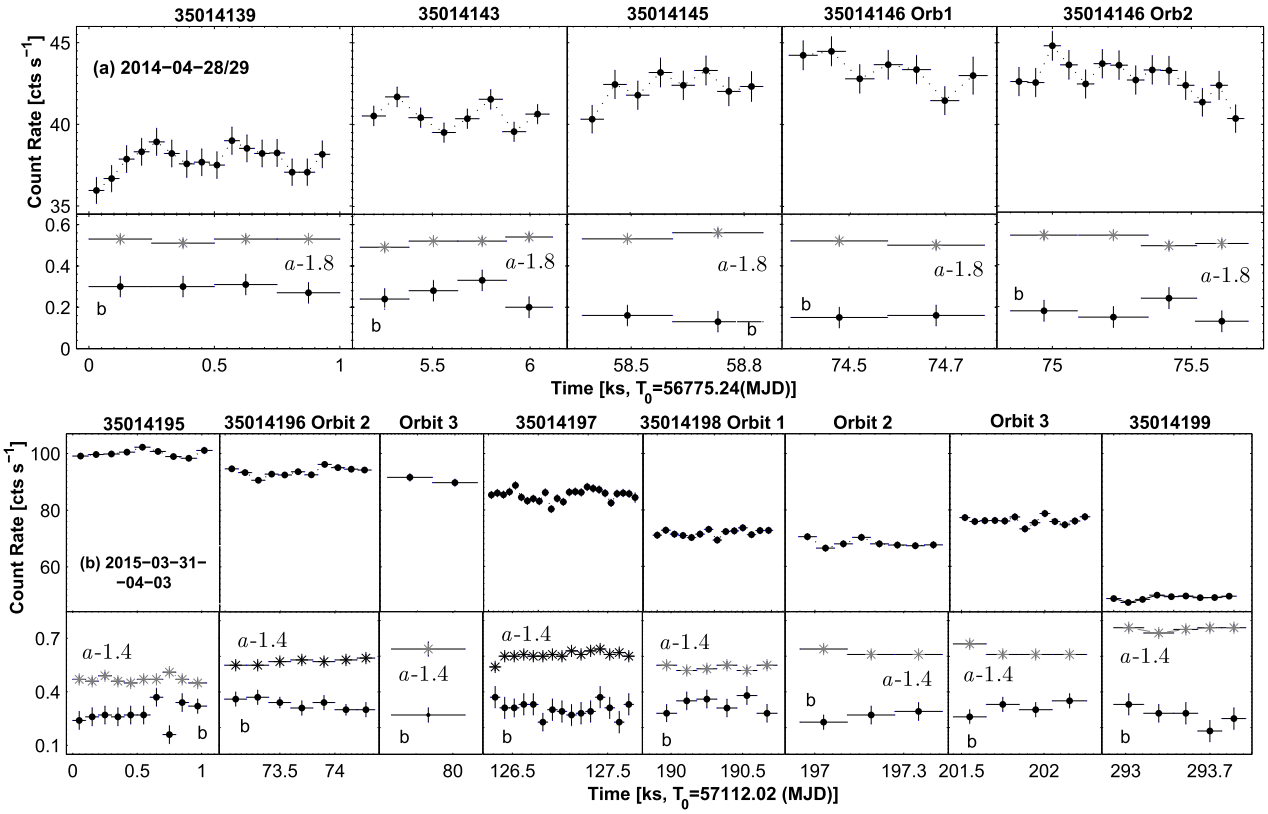

Figure 5. Densely sampled XRT observations of Mrk 421 with a slow variability on intraday timescales.

and did not show extreme spectral features. The distribution peaks are derived via the lognormal fit to the corresponding histograms (Figure 7). For each distribution, we also constructed the corresponding box plot whose left and right borders correspond to the 25% and 75% containments of the values, respectively. The lengths of the left and right whiskers are equal to that of the box plot (i.e., each correspond to the 25% containment of the values).

The curved 0.3–10 keV spectra mostly showed a low value of the curvature parameter b: only 7% of the values from the range $b = 0.08$–0.46 were larger than $b = 0.35$. Note that the spectra from Period 2 showed relatively low curvatures compared to the next period (see Figure 7(a)): the corresponding distribution peak was shifted by $\Delta b = 0.05$ toward the smaller values, and 43% of the values were smaller than $b = 0.20$, while this was the case for 17% of the spectra from Period 3. This fact is reflected in the first panel of Figure 7(a), where the distribution of parameter b is constructed for the whole 2013 November–2015 June period and the histogram shows the two clearly expressed peaks. The mean value of the curvature parameter from each subperiod ranged between $b = 0.20$ (Periods 2a and 3b) and $b = 0.31$ (Period 3e).

Parameter b showed a weak anticorrelation with the position of the SED peak in Period 2 (see Figure 8(a3) and Table 6 for the Spearman correlation coefficient and corresponding p-value), although this analysis was restricted only for the spectra with $E_p \geqslant 0.80$ keV (as explained below). However, these parameters did not exhibit a significant correlation at the 99% confidence level either for Period 3 or for the whole 2013 November–2015 June period (as well as in Period 1a; see Figures 8(a4), (a1), and (a2), respectively). The curvature parameter did not show correlations with the unabsorbed 0.3–10 keV flux and with parameter a either for the data taken as a whole or split into its separate periods, except for Period 3b, which shows a moderate positive a–b correlation and a weak b–flux anticorrelation (see Figures 8(b)–(c) and the corresponding discussion below; both correlations were confirmed by the alternative checks). Parameter b varied on diverse timescales (Figures 9(Ad)–(Bd)) and showed a variability at the 3σ confidence level on intraday timescales several times with $\Delta b = 0.21$–0.26 (along with the 0.3–10 keV IDVs; see Table 3). The fastest variability was an increase by $\Delta b = 0.21$ in 5.5 ks between the second and third orbits of MJD 35,014,120 (see Figure 4(k)) during the flux-halving event.

4.2. Photon Index

The parameter a also showed a very wide range of the values with $\Delta a = 0.94$, with the hardest value of $a = 1.75 \pm 0.02$ (see the Figure 10(b) for the corresponding spectrum), and only 20% of the spectra from the period 2013 November–2015 June were harder than $a = 2$ (Figure 7(b)). Note that the spectra from Period 3 showed a harder distribution compared to the previous period: 99 out of the 107 spectra with $a < 2$, and the distribution peak is shifted by $\Delta a = 0.18$ toward the smaller values (see Table 5, as well as the second and third panels of Figure 7(b)). The positions of the corresponding box plots also clearly show the difference in the distributions. The mean value of this parameter in different subperiods (discussed in Section 3.4) showed the range $\overline{a} = 2.03$–2.12 during Periods 3a–3d (with the hardest value in Period 3c), while $\overline{a} = 2.26$–2.29 (Periods 2b–2d, the softest value in Period 2d). However, even Period 3 showed less extreme values than

Table 3
Summary of the 0.3–10 keV IDVs in 2013 November–2015 June

ObsID(s) (1)	Dates (2)	ΔT (hr) (3)	χ^2/dof (4)	Bin (5)	$F_{\rm var}$(%) (6)	a or Γ (7)	b (8)	$E_{\rm p}$ (keV) (9)	HR (10)
					99.9%				
31202142	2013 Nov 20	1.21	48.83/1	Orbit	4.8(0.9)	2.26(0.02) −2.29(0.03)	0.18(0.07) −0.25(0.05)	0.16(0.05) −0.30(0.06)	0.439(0.016) −0.444(0.024)
35014082	2013 Dec 11	0.28	2.51/16	60 s	2.4(0.5)	2.05(0.02) −2.12(0.03)	0.12(0.05) −0.26(0.05)	0.32(0.05) −0.80(0.10)	0.625(0.021) −0.658(0.024)
35014087	2013 Dec 23	0.27	4.53/7	120 s	4.3(0.9)	2.33(0.02)LP 2.44(0.02)PL	0.15(0.05)	0.08(0.02)	0.392(0.013) −0.424(0.018)
35014091	2014 Jan 02	1.72	193.3/1	Orbit	12.2(0.6)	2.18(0.02) −2.28(0.02)	0.10(0.04) −0.16(0.04)	0.04(0.02) −0.27(0.05)	0.473(0.015) −0.541(0.016)

Note. Column (3) gives the total length of the particular observation (including the intervals between the separate orbits). Column (6) presents the fractional variability amplitude for each IDV. Columns (7)–(10) give the ranges of the photon index, the curvature parameter, the position of the synchrotron SED peak, and the hardness ratio, respectively.

(This table is available in its entirety in machine-readable form.)

Period 1a, with $a_{\rm min} = 1.68 \pm 0.01$, the distribution peak at $a = 1.99$, and 57% of the values harder than $a = 2$.

Figure 8(d1) exhibits an anticorrelation between the parameter a and 0.3–10 keV flux, i.e., the source mostly followed a "harder-when-brighter" trend (see also Figures 9(Ab)–(Bb)). Note that the hardest values harder than $a = 1.90$ correspond to the unabsorbed 0.3–10 keV flux values of $(1.48–3.05) \times 10^{-9}$ erg cm^{-2}s^{-1}, which are a factor of 1.1–2.3 larger than the mean unabsorbed 0.3–10 keV flux value in 2013 November–2015 June, while all the spectra with $a = 2.35–2.69$ yielded fluxes of $(2.78–9.68) \times 10^{-10}$ erg cm^{-2}s^{-1}. This trend was observed in separate Periods 2 and 3, as well as in Period 1a (see Table 5 and Figures 8(d2)–(d4)). As for the subperiods, there was a large difference in Period 2: while we observe a strong anticorrelation with $\rho = 0.85 \pm 0.03$ in Period 2a, this trend was very weak ($\rho = 0.028 \pm 0.13$) in Period 2c. In contrast, the strength of the a–flux anticorrelation did not vary significantly among diverse subperiods of Period 3 ($\rho = 0.57(0.07)$–$0.70(0.04)$). Note also that the data from some observations make a clear exclusion from the general trend (see, e.g., a subsample of seven data points in the lower right part of the third panel, corresponding to the segments of ObsID 35014107 and producing an outlier).

Period 2a exhibited the largest range of the photon index $\Delta a = 0.76$, along with the strongest "harder-when-brighter" trend. This range was also large in Periods 3b and 3e (0.70–0.71), and a weaker spectral variability was observed in other subperiods with $\Delta a = 0.34–0.50$. The photon index often was variable on intraday timescales during the 0.3–10 keV IDVs discussed in Section 3.5 (see Table 3 and Figures 4–6). The largest variability by $\Delta a = 0.36$ (a hardening) in 20.4 hr corresponds to the flux-doubling event on 2014 May 2, and this parameter showed a variability within the 1 ks interval on 2015 January 13 (a hardening by $\Delta a = 0.11$, corresponding to the IDV presented in Figure 4(e)).

The 0.3–10 keV photon index, derived from 28 spectra fitting well with a simple PL, showed a wide range of the values $\Delta\Gamma = 0.86$ and the hardest value $\Gamma = 1.89 \pm 0.01$ (see Figure 10(d) for the corresponding spectrum and Table 7 for the summary of the PL spectra). Note that the majority of these spectra (71%) belong to Period 2. The PL spectra are found in various brightness states, and they followed a "harder-when-brighter" trend stronger than the LP spectra (see Figure 8(e1) and Table 6). A similar situation was also seen in Period 1a (Figure 8(e2)), but the corresponding spectra were, on average, harder ($\Gamma = 1.70–2.35$) and of a higher occurrence (17% vs. 5% in 2013 November–2015 June). Similar to parameter a, the 0.3–10 keV photon index varied on diverse timescales, and it showed the fastest variability on 2015 April 25/26 (MJD 56,773) corresponding to the softening by $\Delta\Gamma = 0.15(0.03)$ in 4.5 hr (Figures 9(Ab)–(Bb)). Similar to Period 1a, some XRT observations showed the presence of both LP and PL spectra extracted from its different segments or orbits. For example, the first orbit of ObsID 35014175 showed a spectral curvature, while the spectrum extracted from the second orbit fits well with the PL model (Figure 10).

4.3. Hardness Ratio and Spectral Hysteresis

The values of the HR, derived from LP and PL spectra, were sped over the wide range ΔHR = 0.922 (Figure 7(f) and Table 5), and only 8 spectra out of 568 showed HR > 1 (see Tables 4 and 7). Figures 10(a)–(b) correspond to the spectra with the highest values of the parameter HR. In Period 1a, 21 spectra (8% of all spectra) showed HR > 1, and 63% of the spectra were harder than HR = 0.7, while 95% and 75% of the HR values were below this threshold in Periods 2 and 3, respectively. The hardest spectra belong to Periods 3a–3c (the mean HR in subperiod $\overline{\rm HR} = 0.645–0.670$), and the softest ones are found in Periods 3b–3c ($\overline{\rm HR} = 0.436–0.451$). A positive correlation between HR and the unabsorbed 0.3–10 keV flux occurred in all periods (see Table 6 and Figure 8(f)), confirming the dominance of a "harder-when-brighter" spectral evolution of Mrk 421 during X-ray flares. In the subperiods, this trend was the strongest in Periods 2a–2b ($\rho = 0.74–0.77$), and it was the weakest in the next two subperiods ($\rho = 0.26–0.30$). Nevertheless, the Spearman coefficient showed even a weaker correlation only at the 97% confidence level in Period 2c, similar to the a–$F_{0.3–10\,\rm keV}$ correlation in the same subperiod.

The HR often varied on intraday timescales during the 0.3–10 keV IDVs (see Table 3). The fastest variability (a decrease by 36% within 1 ks) was associated with the IDV presented in Figure 4(a)), and the largest variability (an increase by 86% in 20.4 hr) was observed on 2014 May 2 during the flux-doubling event (see Section 3.5).

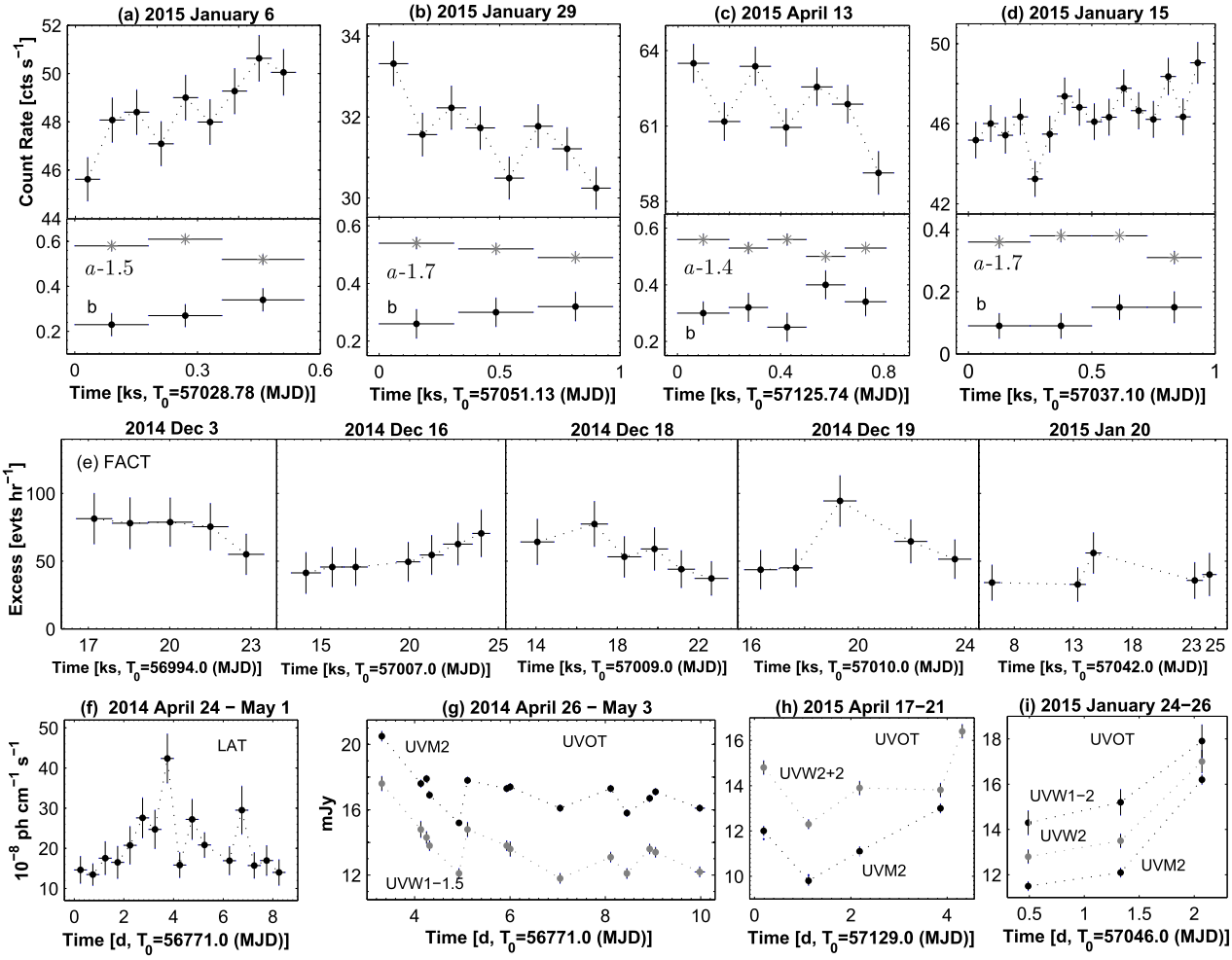

Figure 6. Top row: most notable X-ray IDVs in 2013 November–2015 June detected with 99.5% significance; middle row: FACT light curves of Mrk 421 with 20-minute binning from the most active nights during 2013 November–2015 June; bottom row: LAT-band light curve during 2014 April 24–May 1 constructed using the 0.5-day bins, while each point in the UVOT-band light curves corresponds to the 3 hr bin.

Figure 11 presents an HR–flux plane for Periods 2–3, split into several parts in each period for a better resolution. In Period 2, Mrk 421 exhibited a clockwise (CW) spectral evolution during MJD 56,616–56,644 (Figures 11(a)–(b); the first flare in Period 2a[11]), MJD 56,665–56,681 (Figure 11(c), the epoch after the second flare in Period 2a), MJD 56,695–56,715 (Figure 11(e); the flare in Period 2b), MJD 56,726–56,743 (Figure 11(g); the epoch after the first peak and the second peak in Period 2c), and mostly during MJD 56,771–56,777 (Figure 11(j); the flare in Period d). A counterclockwise (CCW) evolution was evident during MJD 56,644–56,665 (Figure 11(b); the epoch from the declining phase of the first flare and the second flare in Period 2a), MJD 56,681–56,695 (the interval between the start of Period 2b and the flare in this subperiod), MJD 56,716–56,726 (Figure 11(f); the first flare in Period 2c), MJD 56,743–56,756 (the epoch after the second peak in Period 2c), MJD 56,761–56,771 (Figure 11(i); the epoch before the flare in Period 2d), and MJD 56,779–56,781 (Figure 11(k); the declining phase of the flare in Period 2d).

Period 3 was clearly dominated by the CCW-type loops. Namely, they occurred during MJD 57,0141–57,115 (Figures 11(m)–(p); between the second peak in Period 3a and the minimum after the second flare in Period 3c), MJD 57,120–57,154 (Figures 11(r)–11(t); between the start of the first low-amplitude flare and the peak of the fourth one in Period 3d), MJD 57,158–57,164 (Figure 11(t); most of the last flare in Period 3d), and MJD 56,171–57,193 (Figure 11(u); corresponding to the low-amplitude and subsequent strong flares in Period 3e). The opposite loops occurred only during MJD 57,026–57,041 (Figure 11(l); the first flare in Period 3a), MJD 57,154–57,158 (Figure 11(f); a short interval during the fourth low-amplitude flare in Period 3d), and MJD 57,168–57,174 (Figure 11(u)).

4.4. The Position of the SED Peak

The position of the SED peak showed a very wide range between $E_p = 0.005 \pm 0.004$ keV and $E_p = 9.15 \pm 0.94$ keV. However, for the values $E_p \lesssim 0.80$ keV (derived from the X-ray spectral analysis), the position of the synchrotron SED peak is poorly constrained by the XRT observation, and these E_p values should be considered as upper limits to the intrinsic ones (see Kapanadze et al. 2014, 2016b). This is the case for 68% of the LP spectra, and we have not used them when searching for the correlations of E_p with other spectral parameters (or fluxes). Moreover, the SED peaks of the spectra

[11] See the corresponding XRT light curve in Figure 3 when referring to the particular flare in this subsection.

Table 4
Results of the XRT Spectral Analysis with the Log-parabolic Model

ObsID (1)	a (2)	b (3)	E_p (4)	K (5)	χ^2_r/dof (6)	$\log F_{0.3-2\,keV}$ (7)	$\log F_{2-10\,keV}$ (8)	$\log F_{0.3-10\,keV}$ (9)	HR (10)
31202141	2.28(0.02)	0.17(0.04)	0.15(0.04)	0.106(0.001)	1.056/252	−9.470(0.005)	−9.814(0.013)	−9.308(0.006)	0.453(0.015)
31202142 Or1	2.26(0.02)	0.25(0.05)	0.30(0.06)	0.110(0.001)	1.098/223	−9.463(0.005)	−9.821(0.015)	−9.305(0.006)	0.439(0.016)
31202142 Or2	2.29(0.03)	0.18(0.07)	0.16(0.05)	0.118(0.002)	1.159/164	−9.421(0.008)	−9.774(0.022)	−9.261(0.009)	0.444(0.024)
35014077 S1(540 s)	2.28(0.02)	0.22(0.05)	0.23(0.05)	0.140(0.002)	1.128/225	−9.353(0.005)	−9.711(0.015)	−9.195(0.006)	0.439(0.016)

Note. In Column (1), the abbreviations "Or" and "S" stand for "Orbit" and "segment," respectively. The E_p values (Column (4)) are given in keV; unabsorbed 0.3–2 keV, 2–10 keV, and 0.3–10 keV fluxes (Columns (7)–(9))are given in erg cm^{-2} s^{-1}.

(This table is available in its entirety in machine-readable form.)

Table 5
Distribution of Spectral Parameters in Different Periods

Quantity (1)	Min. Value (2)	Max. Value (3)	Peak Value (4)	σ^2 (5)
2013 Nov–2015 Jun				
b	0.08	0.48	⋯	0.006
a	1.75	2.69	⋯	0.025
Γ	1.89	2.75	⋯	0.044
HR	0.221	1.143	⋯	0.023
Period 1a				
b	0.09	0.47	0.20	0.004
a	1.68	2.55	1.99	0.037
Γ	1.70	2.35	⋯	0.027
HR	0.281	1.419	0.720	0.048
Period 2				
b	0.08	0.40	0.19	0.004
a	1.83	2.61	2.24	0.016
Γ	1.89	2.75	⋯	0.047
HR	0.221	1.038	0.442	0.018
Period 3				
b	0.09	0.48	0.24	0.006
a	1.75	2.69	2.06	0.020
Γ	1.89	2.32	⋯	0.028
HR	0.223	1.142	0.555	0.020

Note. Columns (2) and (3): minimum and maximum values, respectively. Column (4): distribution peak. Column (5): variance.

provided in Figures 10(a)–(c) are also poorly constrained by the observational data, and the corresponding values of E_p (7.30–9.15 keV) also should be considered as the upper limits. The vast majority of the spectra with $E_p \geqslant 0.80$ keV belong to Period 3 (163 out of 173 spectra). Only 10 spectra show the position of the synchrotron SED peak in hard X-rays ($E > 2$ keV), including the aforementioned three spectra with highest values of E_p.

The mean value of these parameters in different subperiods (including all available values) ranged between 0.27 keV (Period 2c) and 1.73 keV (Period 3b). For the whole data sets from 2013 November–2015 June and Period 3 (as well in Period 1a), we do not observe a correlation between E_p and the 0.3–10 keV flux, although we observe a positive correlation from the sample taken from Periods 2 and 3c (see Figure 8(g) and Table 6.

Similar to the aforementioned spectral parameters, E_p also varied on various timescales. The most extreme variability was observed during MJD 57,062–57,064, when the position of the synchrotron SED shifted by about 8.5 keV in 2 days toward higher energies (Figure 9(Be)). This event is related to the X-ray flare presented in Figure 3(f), accompanied by the spectral hardening by $\Delta a = 0.36$, by the increase of the HR by a factor of 2.2, and by a decline of the spectral curvature by $\Delta b = 0.23$. Another strong variability by $\Delta E_p > 3.48$ keV was recorded during MJD 56,637.48–56,639.27 (Figure 9(Ae)) in the epoch of the first 0.3–10 keV flare in Period 2a (see Figure 3(a)).

5. Discussion

In this section, we discuss the results from the MWL flux variability and X-ray spectral study of Mrk 421, along with those published to date.

5.1. Flux Variability

5.1.1. Variability Character

During the here-presented 1.6 yr period, Mrk 421 showed a strong X-ray flaring activity by a factor of 1.8–5.2 on timescales of a few weeks and a maximum-to-minimum flux ratio $R \approx 13$. During these flares, the 0.3–10 keV count rate showed a maximum value of 40.1–99.9 counts s^{-1}, and the minimum rates between the flares during Periods 2a–3e were 7.66–31.74 counts s^{-1}. Therefore, Mrk 421 generally was the brightest blazar in the X-ray sky during 2013 November–2015 June. On the other hand, neither the observation-binned nor the 1-minute-binned 0.3–10 keV count rate exceeded 100 counts s^{-1}, while the source often was observed above this level in Period 1a and the 1-minute-binned rate attained the value of 260 counts s^{-1}. Therefore, a strong X-ray flaring activity in Periods 2–3 was relatively modest compared to the giant outburst observed in 2013 April. On average, the source was brighter also in other spectral bands in Period 1a than during Periods 2–3 (see Figure 2), except for the radio band.

Note that the mean 0.3–10 keV rate was 28.50 counts s^{-1} in Period 2, while this quantity was 50% higher in the next period. In the LAT band, the source was detected 3.2 times more frequently in Period 3 and the mean excess rate was 23% larger than in Period 2. In contrast, the largest 0.3–300 GeV fluxes were observed at the end of Period 2, and its mean value was 32% larger than that in the subsequent period. On average, the source was brighter in the ultraviolet UVW1–UVW2 bands in Period 2.

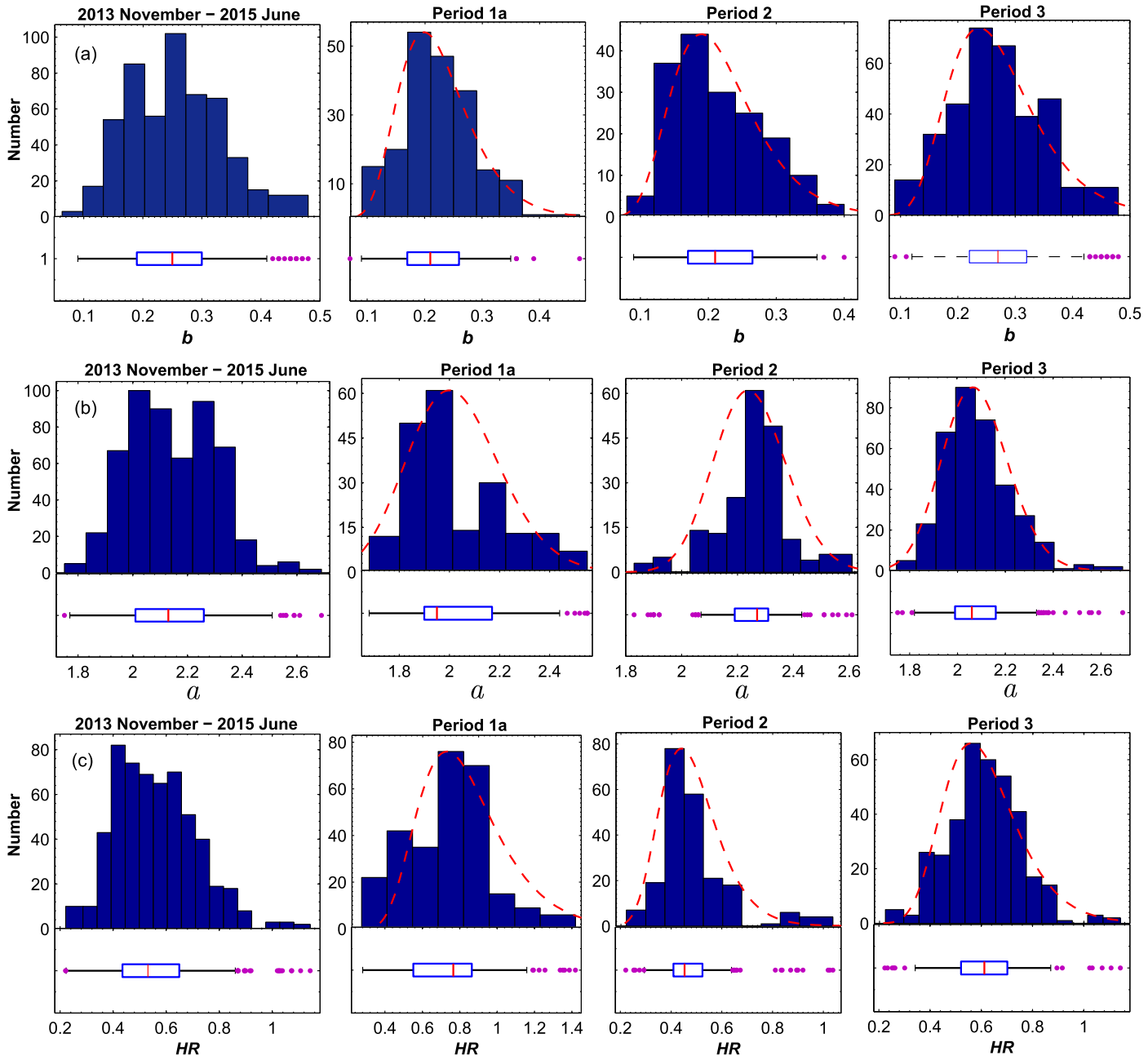

Figure 7. Distribution of the values of spectral parameters in different periods. A red line within each box plot corresponds to the median of the distribution, and the purple points represent the outliers.

Figure 1(a) shows that the source underwent stronger X-ray flaring activity also in 2005–2006, 2008, and 2010 (in addition to that in 2013 April) than in the here-presented 1.6 yr period. In contrast, the *Swift* observations of Mrk 421 in 2007, 2009, and 2011–2012 yielded lower fluxes and significantly weaker X-ray variability. The whole XRT data set of Mrk 421 during 2005–2016 showed a maximum-to-minimum 0.3–10 keV flux ratio $R = 86.5$, and this ratio is significantly larger in the 2–10 keV band ($R = 136.3$), ranging between $(2.88 \pm 0.18) \times 10^{-11}$ erg cm^{-2} s^{-1} and $(3.93 \pm 0.08) \times 10^{-9}$ erg cm^{-2} s^{-1} (2013 January–June; Paper I). Therefore, Mrk 421 is the most violently variable blazar in X-rays. Note that the ratio R from the historical VHE data of Mrk 421 is significantly smaller than in X-rays ($R = 43.4$). In contrast, Mrk 501 and PKS 2155−304 have shown significantly larger overall variability in the VHE band than X-rays (see Kapanadze et al. 2014, 2017a, respectively).

In the $F_{\rm var}$–logν plane, where the $F_{\rm var}$ values from each band are calculated using all the available data obtained with various instruments during 2005–2016, Mrk 421 shows a double-peaked shape with the highest variability in the X-ray and VHE bands (Figure 12(a)). Note that the value of $F_{\rm var}$ is known to be dependent on the data sampling, and this result should be interpreted with caution. Generally, $F_{\rm var}$ was derived using the individual single-day measurements of our target, except for *MAXI* and LAT, for which, because of the limited sensitivity, we used data integrated over 1 week, and for the calculation of fractional variability amplitude from the *MAXI*, BAT, and LAT observations, we used only the flux values from those time bins when the source was detected with the significances described

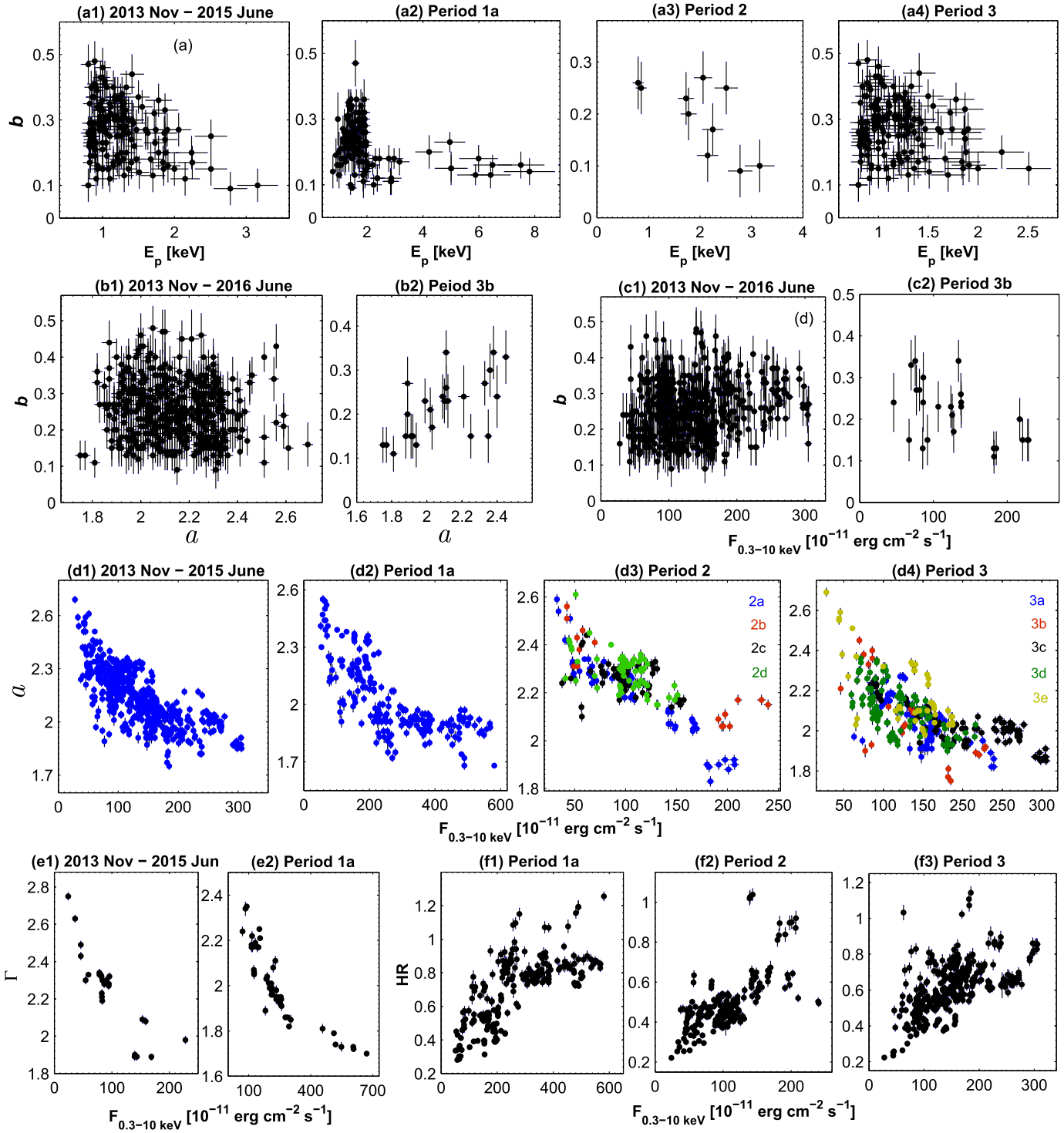

Figure 8. Correlation between the spectral parameters and fluxes. The colored points in the third and fourth panels of Figure 8(d) correspond to different subperiods of Periods 2–3.

in Sections 2.1–2.2. A similar shape is evident from Figure 12 (c)–(d), where a $\log \nu$–$F_{\rm var}$ plot is constructed separately for Periods 2 and 3, and the 2-day binned LAT fluxes are used to derive the fractional variability amplitude. Note that the BAT data point was not available for these periods. A similar shape is evident also in the epoch of a giant X-ray outburst (Figure 12(b)). Note that Figure 12(a) showed larger values of $F_{\rm var}$ in the optical V and R bands. This result should be related to the strong optical flares in some epochs when no contemporaneous *Swift* observations were carried out (see Figures 1(g)–(h)). This shape, exhibiting the highest variability in the X-ray and VHE bands, was interpreted as resulting from a correlation between the synchrotron and IC peaks by Furniss et al. (2015), and as an indication that the electron energy distribution is most variable at the highest energies (within the one-zone SSC scenario; see Alecsic et al. 2015b). Although a limited sensitivity and the use of larger time bins can underestimate $F_{\rm var}$ values for some instruments, a double-peak

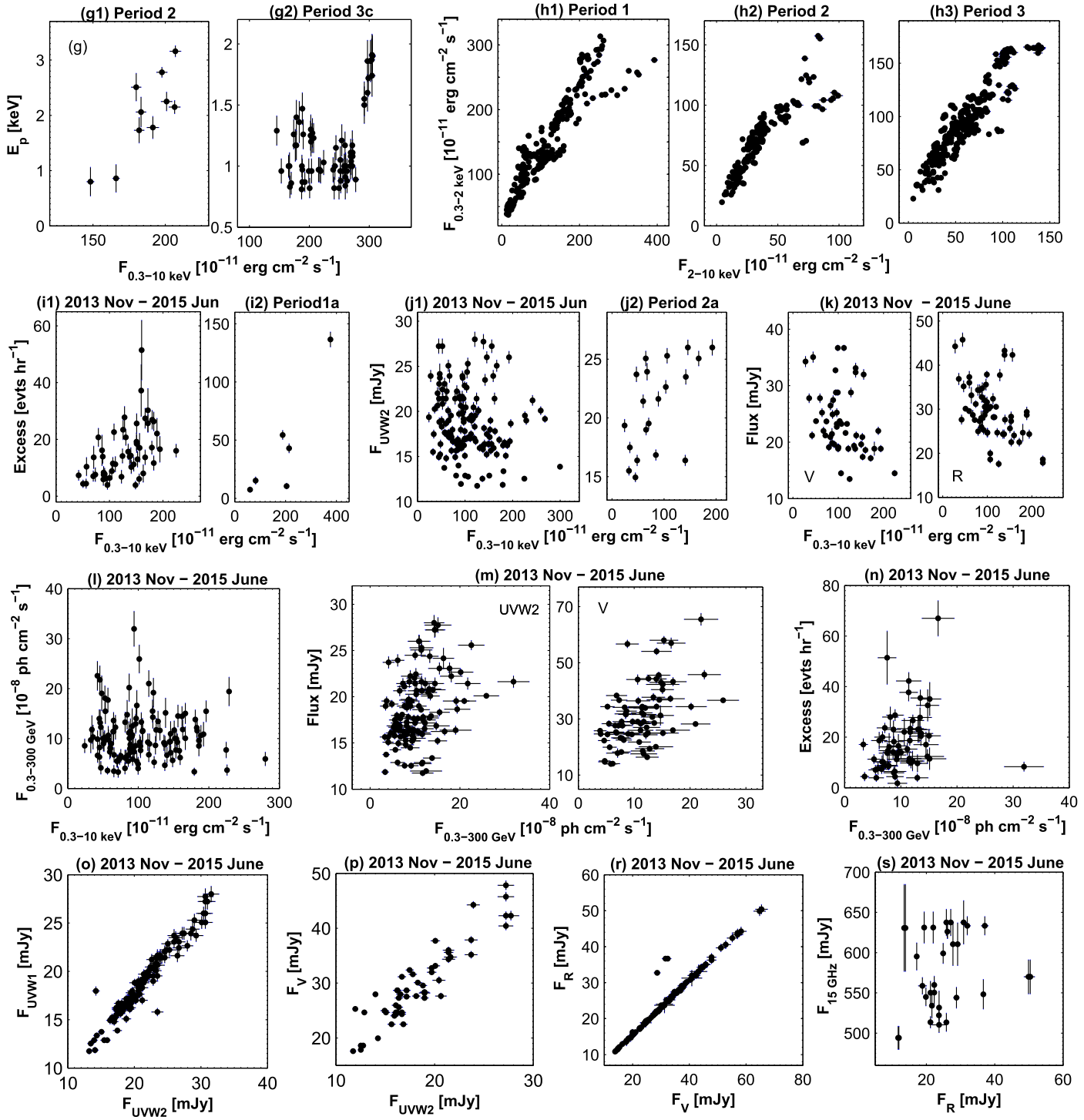

Figure 8. (Continued.)

shape in the F_{var}–logν plane seems to be inherent for HBLs, and it has been reported by various authors for Mrk 421 from the MWL campaign performed in various epochs (Paper I; Alecsic et al. 2015b; Ahnen et al. 2016; Balocovic et al. 2016) and for Mrk 501 in 2014 March–October (Kapanadze et al. 2017a). The principal component analysis confirms that the maximum contribution in the MWL flux variability of our target is made by those observed at X-ray and VHE frequencies (in the whole period 2005–2016, as well as in the separate periods).

5.1.2. Flux Variability on Intraday Timescales

During 2013 November–2015 June, our target was active also on intraday timescales, and the corresponding duty cycle (DC, i.e., the fraction of total observation time during which the object displays a variability; Romero et al. 1999) of the 0.3–10 keV IDVs detected with the 99.9% confidence level is 46%. Therefore, Mrk 421 was significantly less variable on intraday timescales in this period than during 2013 January–April, when DC = 83% from the XRT observations, and this

Table 6
Correlations between the Spectral Parameters and MWL Fluxes (Denoted by "F_i" for the Particular i Band) in Different Periods

Quantities	ρ	p
2013 Nov–2015 Jun		
a and $F_{0.3-10\,\mathrm{keV}}$	−0.70(0.05)	3.04×10^{-12}
Γ and $F_{0.3-10\,\mathrm{keV}}$	−0.77(0.05)	6.81×10^{-12}
HR and $F_{0.3-10\,\mathrm{keV}}$	0.69(0.05)	1.24×10^{-12}
$F_{0.3-2\,\mathrm{keV}}$ and $F_{2-10\,\mathrm{keV}}$	0.87(0.03)	$<10^{-15}$
$F_{0.3-10\,\mathrm{keV}}$ and F_{FACT}	0.35(0.12)	8.85×10^{-4}
F_{V} and $F_{0.3-10\,\mathrm{keV}}$	−0.35(0.11)	8.07×10^{-4}
F_{R} and $F_{0.3-10\,\mathrm{keV}}$	−0.33(0.11)	4.54×10^{-3}
F_{UVW2} and $F_{0.3-300\,\mathrm{GeV}}$	0.37(0.09)	4.81×10^{-5}
F_{UVM2} and $F_{0.3-300\,\mathrm{GeV}}$	0.36(0.09)	5.15×10^{-5}
F_{UVW1} and $F_{0.3-300\,\mathrm{GeV}}$	0.31(0.10)	8.89×10^{-4}
F_{FACT} and $F_{0.3-300\,\mathrm{GeV}}$	0.35(0.12)	3.57×10^{-3}
F_{V} and $F_{0.3-300\,\mathrm{GeV}}$	0.48(0.09)	4.04×10^{-7}
F_{R} and $F_{0.3-300\,\mathrm{GeV}}$	0.45(0.09)	2.40×10^{-6}
F_{UVW1} and F_{UVM2}	0.85(0.03)	$<10^{-15}$
F_{UVW1} and F_{UVW2}	0.91(0.02)	$<10^{-15}$
F_{UVM2} and F_{UVW2}	0.86(0.03)	$<10^{-15}$
F_{UVW2} and F_{V}	0.85(0.03)	$<10^{-15}$
F_{UVM2} and F_{V}	0.83(0.03)	$<10^{-15}$
F_{UVW1} and F_{V}	0.86(0.03)	$<10^{-15}$
F_{UVW2} and F_{R}	0.73(0.05)	2.22×10^{-13}
F_{UVM2} and F_{R}	0.70(0.05)	3.45×10^{-13}
F_{UVW1} and F_{R}	0.74(0.05)	1.79×10^{-13}
F_{V} and F_{R}	0.95(0.02)	$<10^{-15}$
Period 1a		
a and $F_{0.3-10\,\mathrm{keV}}$	−0.61(0.05)	1.03×10^{-11}
Γ and $F_{0.3-10\,\mathrm{keV}}$	−0.79(0.04)	3.47×10^{-12}
HR and $F_{0.3-10\,\mathrm{keV}}$	0.61(0.06)	1.023×10^{-10}
$F_{0.3-2\,\mathrm{keV}}$ and $F_{2-10\,\mathrm{keV}}$	0.86(0.03)	$<10^{-15}$
Period 2		
b and E_{p}	−0.46(0.15)	3.35×10^{-4}
a and $F_{0.3-10\,\mathrm{keV}}$	−0.66(0.05)	3.00×10^{-11}
HR and $F_{0.3-10\,\mathrm{keV}}$	0.58(0.06)	9.99×10^{-10}
E_{p} and $F_{0.3-10\,\mathrm{keV}}$	0.65(0.11)	8.80×10^{-5}
$F_{0.3-2\,\mathrm{keV}}$ and $F_{2-10\,\mathrm{keV}}$	0.80(0.04)	$<10^{-15}$
F_{UVW1} and $F_{0.3-10\,\mathrm{keV}}$ (2a)	0.54(0.12)	1.02×10^{-4}
F_{UVW2} and $F_{0.3-10\,\mathrm{keV}}$ (2a)	0.43(0.14)	4.45×10^{-4}
F_{UVW2} and $F_{0.3-10\,\mathrm{keV}}$ (2a)	0.45(0.14)	2.99×10^{-4}
Period 3		
b and $F_{0.3-10\,\mathrm{keV}}$ (Period 3b)	−0.45(0.14)	9.36×10^{-4}
a and b (Period 3b)	0.56(0.12)	1.10×10^{-5}
a and $F_{0.3-10\,\mathrm{keV}}$	−0.67(0.05)	2.42×10^{-11}
HR and $F_{0.3-10\,\mathrm{keV}}$	0.61(0.06)	7.67×10^{-11}
E_{p} and $F_{0.3-10\,\mathrm{keV}}$ (Per 3c)	0.29(0.11)	1.09×10^{-3}
$F_{0.3-2\,\mathrm{keV}}$ and $F_{2-10\,\mathrm{keV}}$	0.87(0.03)	$<10^{-15}$

quantity almost amounted to 100% during the *NuSTAR* campaign. Note that this result can be partially related to significantly more densely sampled observations in the latter period (especially during the giant outburst) and to the increasing variability strength with frequency (see Section 5.1.1). However, the extreme IDVs in 2013 January–April showed the flux-doubling/halving timescales $\tau_{\mathrm{d,h}} = 1.04$–$7.20$ hr and $\tau_{\mathrm{d,h}} = 1.16$–$2.74$ hr in the XRT and *NuSTAR* bands, respectively, while the source showed only single flux-doubling and flux-halving events during the ∼11 months of the XRT observations during Periods 2–3. These events yielded $\tau_{\mathrm{d}} = 20.1$ hr and $\tau_{\mathrm{h}} = 2.6$ hr (calculated via the equation $\tau_{\mathrm{d,h}} = \Delta t \times \ln(2)/\ln(F_2/F_1)$; Saito et al. 2013). The largest IDV incorporated a flux change by a factor of 2.2 during the densely sampled XRT observation presented in Figure 4(k), while significantly more extreme variability was recorded several times in Period 1a (e.g., a flux increase by a factor of 6.28–8.84 within 1 day on 2013 April 11/12; see Paper I). Note also that the source sometimes varied very slowly on intraday timescales during the densely sampled XRT observations in the latter period (see Figure 5), while similar cases were not observed in 2013 January–April.

It is important to check an occurrence of IDVs in different brightness states that can hint at the possible underlying unstable mechanisms. Namely, the IDVs observed during flaring epochs are in favor of the shock-in-jet scenario (interaction of a propagating shock front with the jet inhomogeneities; Sokolov et al. 2004), while those caused by other mechanisms occurring in the innermost blazar area should be more conspicuous when the source is relatively faint, i.e., the variable emission from the black hole vicinity will not be "shadowed" by the huge amount of the flux generated by the emission zone following the shock front (see, e.g., Mangalam & Wiita 1993; Kapanadze et al. 2014). Similar to Period 1a, most of 0.3–10 keV IDVs were observed in higher brightness states in Period 3 (see Figures 12(a) and (c)), while the source showed the majority of its IDVs during fainter states in Period 2. Therefore, the unstable mechanisms, occurring in the innermost AGN area, could be more important for the generation of the variable X-ray emission on intraday timescales in the latter period.

5.2. Interband Cross-correlations

5.2.1. Soft–Hard X-Rays and X-Ray–TeV Correlation

The unabsorbed soft 0.3–2 keV flux showed a strong positive correlation with the hard 2–10 keV flux in all periods, being perhaps a bit weaker in Period 2 (see Table 6 and Figure 8(h)). The data from some particular observation show an exclusion from the general trend and produce outliers in the scatter plots. A strong $F_{0.3-2\,\mathrm{keV}}$–$F_{2-10\,\mathrm{keV}}$ correlation was observed also in all subperiods, and the corresponding light curves mostly followed each other closely. However, the hard flux varied by a larger amplitude than the soft one in each period (see Table 3 and Figure 11), yielding a strong spectral variability. This difference was especially large in Period 3d, when the 0.3–2 keV flux varied by a factor of 5.6, while we observe a variability by a factor of 22.7 in the 2–10 keV band. For the whole 2013 November–2015 June period, a maximum-to-minimum flux ratio in the 2–10 keV flux $R = 32.25$, while $F^{\mathrm{max}}_{0.3-2\,\mathrm{keV}}/F^{\mathrm{min}}_{0.3-2\,\mathrm{keV}} = 8.45$.

Figure 8(i1) shows the presence of a weak positive correlation between the 0.3–10 keV flux and FACT excess rate during 2013 November–2015 June. Although we observe a strong X-ray–TeV correlation in Period 1a with $\rho = 0.74$, there are few data points in the corresponding scatter plot, and the significance of this correlation is lower than the 99% confidence level (see Figure 8(i2) and Table 6). Note that the source exhibited an uncorrelated X-ray–TeV variability in

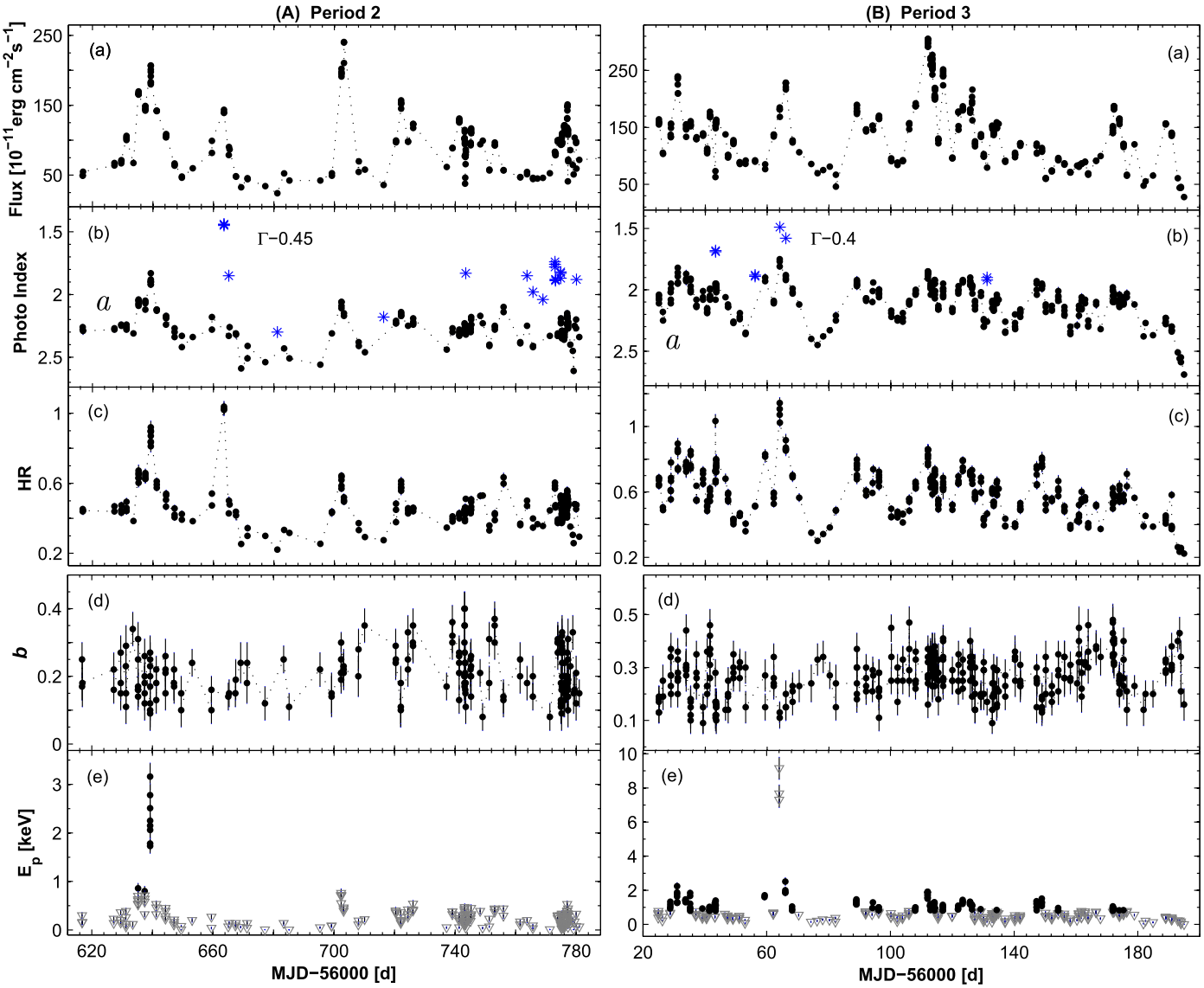

Figure 9. (a) Unabsorbed 0.3–10 keV flux, (b) photon index, (c) HR, (d) curvature parameter, and (e) E_p in 2013 November–2015 June as a function of time.

some occasions during Periods 2–3, namely, a strong TeV flare by a factor of 13 with a peak on MJD 57,044 was not accompanied by significant activity in the XRT band (Figure 3(e)). A similar situation occurred during MJD 57,091–57,096 (Figure 3(g)), and a strong TeV flare by a factor of 6.8 during MJD 57,120–57,128 was accompanied only by a low-amplitude X-ray flare (Figure 8(h)). On the contrary, the source was not detectable by FACT or showed a low TeV state during the second, lower-amplitude flare and the subsequent strong X-ray flare in Period 3e (Figure 3(i)). Furthermore, there was a VHE decline during the increase phase of the strong X-ray flare in Period 2b (Figure 3(b)). The FACT-band brightness showed some decline along with a flare peak and then showed a fast increase by 75% in about 1 day in Period 3d (Figure 3(f)), which is difficult to explain via the one-zone SSC scenario (see Blazejowski et al. 2005). The source was not observed by FACT during the strong X-ray flares in Periods 2a, 2c, 2d, 3a, and 3e, which also contributed to the weakness of the X-ray–TeV correlation.

Uncorrelated X-ray and TeV variabilities also occurred in the past. The MWL campaign in 2002 December–2003 January revealed a rather loose correlation between the X-ray and TeV fluxes, although there was also a very strong X-ray flare by a factor of 7 within 3 days, not accompanied by a comparable TeV counterpart (Rebillot et al. 2006). The TeV flux reached its peak days before the X-ray flux during the giant flare in 2004 that was impossible to explain via the standard one-zone SSC model, and Blazejowski et al. (2005) suggested this as an instance of an "orphan" TeV flare. Acciari et al. (2011) also found high X-ray states, not accompanied by TeV flaring and vice versa in 2006–2008.

5.2.2. X-rays versus HE and Optical–UV Emissions

The 0.3–10 keV flux generally showed an uncorrelated behavior with the UVOT-band fluxes during 2013 November–2015 June (similar to Period 1a), except for Period 2a, when a positive correlation between these quantities was observed (Figure 8(j)). In contrast, the 0.3–10 keV flux showed an anticorrelation with the *V*- and *R*-band fluxes during 2013 November–2015 June (Figure 8(k)). As we have seen in Section 3.4, the optical–UV band light curves sometimes showed a decline when the source had undergone an X-ray

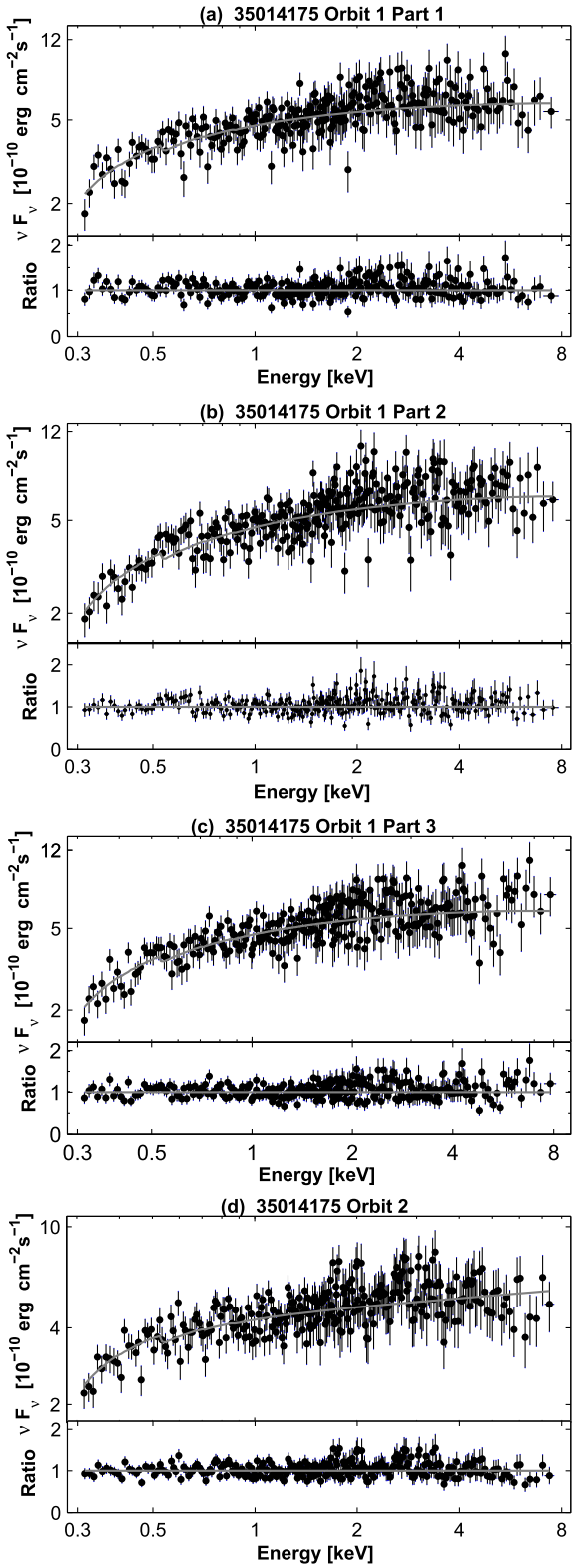

Figure 10. Most extreme spectra of Mrk 421 during 2013 November–2015 June from ObsID 35014175 (2015 February 11, MJD 57,064; along with the distribution of the residuals). Figures (a)–(c) correspond to the three 200 s segments of the first orbit of this XRT observation, which fit well with the LP model yielding $a = 1.75(0.02)$–$1.81(0.02)$, $b = 0.11(0.04)$–$0.13(0.04)$, $E = 7.30(0.75)$–$9.15(0.94)$ keV, HR $= 1.072(0.032)$–$1.143(0.034)$, and $\chi^2_{\rm r} = 1.006$–1.135 with 263–276 dof. The bottom spectrum is extracted from the second orbit of the same observation, described well with a simple PL with $\Gamma = 1.89(0.01)$, HR $= 1.023(0.024)$, and $\chi^2_{\rm r} = 0.921$ with 276 dof.

flare. Note that a negative $F_{0.3-10\,\rm keV}$–$F_{\rm UV}$ trend was observed in all UVOT bands in Periods 2c and 3b, but these anticorrelations were slightly below the 99% confidence level. A similar situation was reported by Alecsic et al. (2015a) for Mrk 421 from the MWL campaign in 2009 January–June. They explained it via the hardening in the electron energy distribution that can shift the entire synchrotron bump to higher energies. Our results and the trend of shifting the synchrotron SED peak position toward higher energies with the increasing X-ray flux (see Section 4.4) also favor this scenario.

During the whole 2013 November–2015 June period, the source did not show a correlation between the 0.3–10 keV and 0.3–300 GeV fluxes, while the latter was correlated with the UVOT-band fluxes (see Figures 8(l)–(m)). This result is expected owing to the effect of the Klein-Nishina (KN) suppression in the IC process, leading to the efficient upscatter of the optical–UV photons at the GeV energies by the electrons radiating at X-rays (Tramacere et al. 2009, hereafter T09). However, we observe a positive correlation between the XRT- and LAT-band fluxes for the sample taken from Period 2b separately (the second panel of Figure 8(l); confirmed also by alternative checks). Note that this subperiod does not exhibit any positive HE–optical or HE–UV trends, and we suggest that the upscatter of X-ray photons to the MeV/GeV energies in the KN regime possibly was more efficient in this subperiod than the upscatter of UV photons to these energies in the Thomson regime.

Figure 8(n) demonstrates a weak positive correlation between the FACT- and LAT-band emissions. However, the data points with MJD 56,753 (corresponding to the strong LAT-band flare at the end of Period 2c; the lower right point) and MJD 57,044 (the peak of a TeV flare in Period 3a; the upper left point) produce outliers from the scatter plot $F_{0.3-300\,\rm GeV}$–$F_{\rm FACT}$. They hint at different origins of the LAT- and FACT-band emissions in the epochs of those strong γ-ray flares.

The optical–UV fluxes showed strong or very strong correlations to each other in all periods (see Table 6, Figures 8(o)–(r)) and did not exhibit any features hinting that these originate from different electron populations. In contrast, the 15 GHz flux from the OVRO observations does not show a correlation with that from any band (see, e.g., the scatter plot $F_{\rm UVW2}$–$F_{15\,\rm GHz}$ in Figure 8(s)), indicating its generation in a different jet area. Note that the principal component analysis of simultaneous MWL data shows an increase by about 5% in the proper variance of the first basis vector if we remove the radio data from the analysis, confirming its origin from the lepton population, different from that responsible for the energy "budget" in other spectral bands.

5.3. Spectral Curvature

The origin of X-ray spectral curvature is related to the curved spectral distribution of the electrons with energy, produced by various acceleration mechanisms. According to M04, the LP spectrum of the electrons can be established at the shock front propagating in a medium where the electrons are confined by a magnetic field with a confinement efficiency decreasing with an increasing gyroradius. In that case, the probability $p_{\rm i}$ of a particle's subsequent acceleration at step i is related to its Lorentz factor $\gamma_{\rm i}$ (i.e., to its energy) as $p_{\rm i} = g/\gamma_{\rm i}^q$, where g and q are constants. If $q > 0$, the probability of subsequent

Table 7
Results of the XRT Spectral Analysis with a Simple PL Model

ObsID (1)	Γ (2)	K (3)	χ^2/dof (4)	log $F_{0.3-2\,\mathrm{keV}}$ (5)	log $F_{2-10\,\mathrm{keV}}$ (6)	log $F_{0.3-10\,\mathrm{keV}}$ (7)	HR (8)
35014092 S1 (180 s)	1.89(0.02)	0.238(0.003)	1.007/219	−9.152(0.006)	−9.136(0.011)	−8.843(0.006)	1.038(0.030)
35014092 S2 (170 s)	1.90(0.02)	0.232(0.003)	1.06/211	−9.162(0.007)	−9.154(0.012)	−8.897(0.007)	1.019(0.033)
35014092 S1 (175 s)	1.89(0.02)	0.233(0.003)	1.013/214	−9.162(0.007)	−9.151(0.012)	−8.855()0.006	1.026(0.033)
35014093 Or2	2.30(0.02)	0.181(0.003)	0.946/106	−9.22(0.008)	−9.520(0.016)	−9.044(0.007)	0.501(0.021)
35014099	2.75(0.02)	0.049(0.001)	1.128/143	−9.705(0.007)	−10.360(0.016)	−9.618(0.006)	0.221(0.009)
35014111	2.63(0.02)	0.074(0.001)	1.066/174	−9.550(0.006)	−10.110(0.013)	−9.444(0.005)	0.275(0.009)
35014121 4 S2(400 s)	2.28(0.02)	0.173(0.019)	1.068/214	−9.244(0.006)	−9.531(0.011)	−9.063(0.005)	0.511(0.015)
35014132 S2(560 s)	2.30(0.02)	0.109(0.012)	1.067/215	−9.440(0.005)	−9.739(0.011)	−9.263(0.005)	0.501(0.014)
35014133 S1(530 s)	2.43(0.02)	0.095(0.001)	1.165/194	−9.482(0.006)	−9.881(0.012)	−9.336(0.005)	0.399(0.012)
35014135	2.49(0.02)	0.095(0.001)	1.017/202	−9.469(0.005)	−9.918(0.011)	−9.337(0.005)	0.356(0.010)
35014137 S1(335 s)	2.19(0.02)	0.162(0.002)	1.049/218	−9.284(0.006)	−9.503(0.011)	−9.079(0.005)	0.604(0.017)
35014137 S2(335 s)	2.21(0.02)	0.162(0.002)	1.084/212	−9.282(0.006)	−9.514(0.011)	−9.082(0.005)	0.586(0.017)
35014137 S3(335 s)	2.23(0.02)	0.162(0.002)	1.062/215	−9.279(0.006)	−9.523(0.011)	−9.083(0.005)	0.570(0.016)
35014138 Or1 S1(410 s)	2.34(0.02)	0.159(0.002)	0.950/221	−9.271(0.005)	−9.606(0.010)	−9.106(0.005)	0.462(0.012)
35014138 Or1 S2(410 s)	2.33(0.02)	0.158(0.002)	0.958/221	−9.274(0.004)	−9.598(0.011)	−9.106(0.005)	0.474(0.013)
35014138 Or2	2.33(0.02)	0.163(0.002)	1.071/200	−9.261(0.006)	−9.586(0.012)	−9.093(0.005)	0.473(0.015)
35014140 Or1 S1(350 s)	2.32(0.02)	0.193(0.002)	0.892/225	−9.191(0.005)	−9.506(0.01)	−9.019(0.005)	0.484(0.013)
35014140 Or1 S2(350 s)	2.28(0.02)	0.189(0.002)	1.005/225	−9.204(0.005)	−9.489(0.010)	−9.023(0.005)	0.519(0.013)
35014140 Or1 S3(340 s)	2.27(0.02)	0.188(0.002)	0988/224	−9.210(0.005)	−9.486(0.011)	−9.025(0.005)	0.529(0.015)
35014152	2.33(0.01)	0.119(0.001)	0.977/205	−9.397(0.006)	−9.719(0.012)	−9.227(0.005)	0.476(0.015)
35014165 Or2 S1(160 s)	2.08(0.02)	0.295(0.004)	0.977/208	−9.038(0.006)	−9.173(0.012)	−8.799(0.006)	0.733(0.023)
35014165 S2(160 s)	2.09(0.02)	0.285(0.004)	1.014/206	−9.052(0.006)	−9.190(0.012)	−8.815(0.006)	0.728(0.023)
35014172 S1(240 s)	2.28(0.02)	0.184(0.002)	0.985/190	−9.215(0.006)	−9.503(0.013)	−9.035(0.006)	0.515(0.017)
35014172 S2(240 s)	2.29(0.02)	0.190(0.002)	0.849/183	−9.226(0.007)	−9.518(0.013)	−9.047(0.006)	0.511(0.018)
35014175 Or2	1.89(0.01)	0.281(0.003)	0.921/276	−9.079(0.005)	−9.069(0.009)	−8.773(0.005)	1.023(0.024)
35014176 S2(200 s)	1.98(0.02)	0.403(0.005)	1.044/215	−8.914(0.006)	−8.974(0.012)	−8.642(0.006)	0.871(0.027)
35014210 S1(200 s)	2.30(0.02)	0.168(0.002)	1.144/127	−9.254(0.007)	−9.555(0.015)	−9.078(0.007)	0.500(0.019)
35014210 S2(200 s)	2.32(0.02)	0.165(0.003)	0.995/129	−9.256(0.008)	−9.575(0.015)	−9.086(0.007)	0.480(0.019)

Note. In Column (1), the abbreviations "Or" and "S" stand for "orbit" and "segment," respectively. Unabsorbed 0.3–2 keV, 2–10 keV, and 0.3–10 keV fluxes (Columns (5)–(7)) are given in erg cm^{-2} s^{-1}.

(This table is available in machine-readable form.)

acceleration becomes gradually lower as the energy increases, and this may cause the establishment of the LP energy spectrum of relativistic electrons (so-called energy-dependent acceleration probability process, EDAP). In the framework of EDAP, a positive correlation between the parameters a and b is expected, which was the case only for the 0.3–10 keV flare observed in Period 3b (see Section 4.1). A similar result was reported by M04 for our target from the *BeppoSAX* observations in 1997–1999 (with a stronger a–b correlation than in Period 3b). Other bright HBLs (1ES 1959+650, Mrk 501, PKS 2155−304) did not exhibit an importance of EDAP during the X-ray flares (see Kapanadze et al. 2014, 2016b, 2017a, 2017b).

On the other hand, a curved spectral distribution can be established via the stochastic acceleration arising from the magnetic turbulence close to the shock front (T09). Massaro et al. (2011) demonstrated that the electrons in the jets of TeV-detected HBLs should undergo a more efficient stochastic acceleration than in those of the TeV-undetected HBLs, and the synchrotron SEDs are expected to be relatively broad (i.e., the curvature is smaller with $b \backsimeq 0.3$) in that case, while they become narrower ($b \backsimeq 0.7$) in the opposite case. As discussed in Section 4.1, the curvature parameter was mostly smaller than 0.35 in both Periods 2 and 3 (similar to Period 1a) and showed an anticorrelation with the parameter $E_{\rm p}$, expected in the case of effective stochastic acceleration. It is possible that this mechanism was more important in Period 2, exhibiting stronger b–$E_{\rm p}$ anticorrelation than in Period 3. However, this period is characterized by a significantly poor data set used for the construction of the corresponding scatter plot (due to use of the subsample with $E_{\rm p} \geqslant 0.8$ keV for this purpose), and we cannot draw a firm conclusion about the more effective stochastic acceleration in this period.

Although parameter b varied on various timescales in Periods 2–3 and we found one case of the intraday variability of this parameter, it was less extreme than that in Period 1a, when the spectral curvature varied several times within 1 ks (see Paper I).

5.4. Spectral Hysteresis

The analysis of hysteresis patterns in the HR–flux plane is a useful tool for drawing conclusions related to the interplay between electron acceleration ($\tau_{\rm acc}$), synchrotron cooling ($\tau_{\rm syn}$), and flux variability ($\tau_{\rm var}$) timescales. In this plane, the following patterns are expected (Cui 2004): (a) A CW loop, if $\tau_{\rm syn} \gg \tau_{\rm var} \gg \tau_{\rm acc}$, or $\tau_{\rm syn} \gg \tau_{\rm acc} \gg \tau_{\rm var}$. The spectral evolution should be due to the flaring component starting in the hard X-ray band, triggered by a rapid injection of very energetic particles rather than by a gradual acceleration, and a soft lag is expected (T09). The spectrum is expected to become

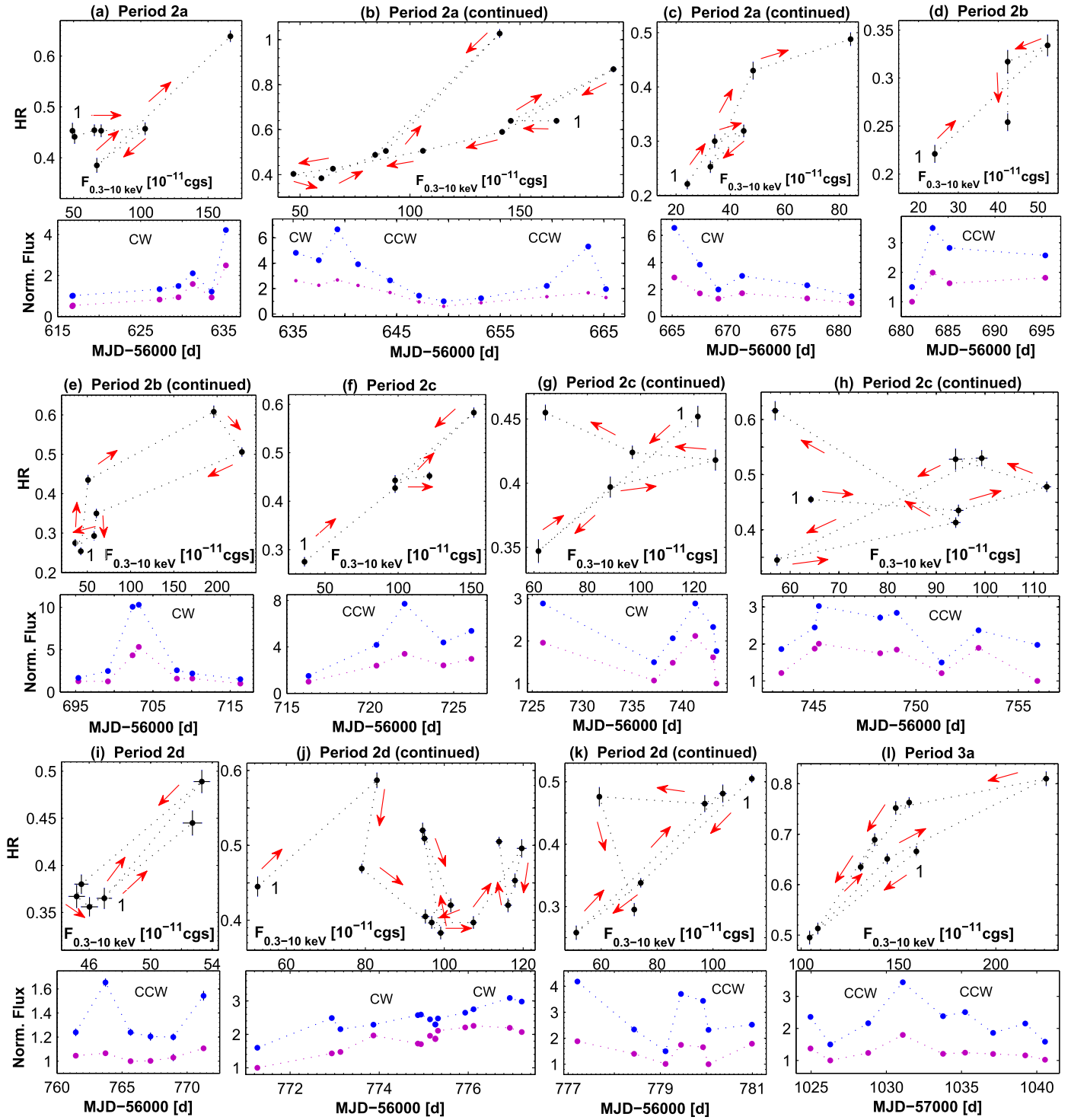

Figure 11. Spectral hysteresis in different epochs, along with the normalized soft 0.3–2 keV (purple points) and hard 2–10 keV (blue points) fluxes plotted vs. time. The light curves for hard fluxes are shifted arbitrarily for a better resolution. In each panel, the start point is denoted by "1." The abbreviation "cgs" stands for erg cm^{-2} s^{-1}.

steeper in the declining phase of the source and harder in the brightening phase, indicating that the hard X-ray variability leads that in the soft X-rays during both the increase and the decrease of brightness (Takahashi et al. 1996). (b) A CCW loop, when $\tau_{syn} \approx \tau_{acc} \approx \tau_{var}$. The information about the occurrence of a flare propagates from lower to higher electron energies, as they are gradually accelerated, while the brightness decline epoch can be dominated by the particle escape effects, and we therefore should observe a hard lag (Ravasio et al. 2004).

Our study of the hysteresis patterns in Mrk 421 shows that the strong X-ray spectral variability during the flares, which occurred in our target during the 1.6 yr period, exhibited various interplays between electron acceleration, synchrotron cooling, and flux variability timescales. The flares in Period 3 mostly showed CW loops in the HR–flux plane, and this result

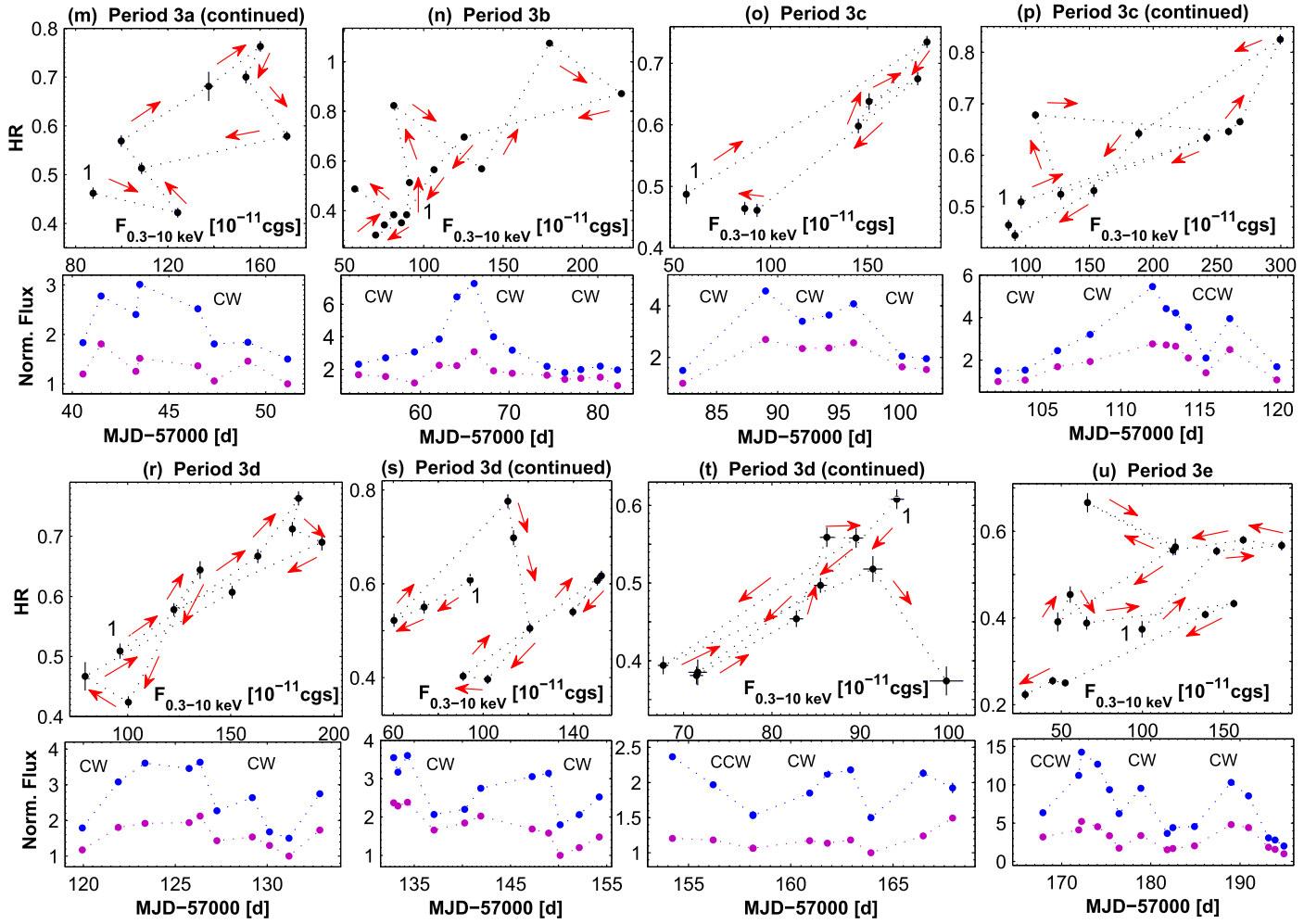

Figure 11. (Continued.)

is consistent with the dominance of synchrotron cooling, since its timescale is shorter at higher energies (Falcone et al. 2004). We observe a possible soft delay on MJD 57,035 (Figure 11(l)), MJD 57,064 (Figure 11(n)), MJD 57,094 (Figure 11(o)), MJD 57,112 (Figure 11(p)), and MJD 57,168 (Figure 11(t)). However, the XRT observations of Mrk 421 are not suitable for using the local cross-correlation function (LCCF; Max-Moerbeck et al. 2014) to estimate the significances and derive exact values of these delays: the duration of each observation generally was much shorter than the time intervals between them.

The situation was more complex in Period 2 when the CW- and CCW-type spectral evolutions changed each other even in the course of some short-term flares, although pure CW and CCW loops are also observed. Our HR–flux planes exhibit many cases when the spectrum started to become harder, while the 0.3–10 keV or the 3–79 keV flux was still decreasing (see Figures 11(g)–(h), (j), (m), (u)), which may indicate the propagation of a new injection from the hard band, as the soft band is still decreasing (T09).

From the past X-ray studies of Mrk 421, pure CW and CCW loops, or the changes from the CW-type spectral evolution into opposite one and vice versa during 2013 January–May was reported in Paper I. However, clearly expressed CW or CCW loops during some 0.3–10 keV IDVs were seen in this period, in contrast to Periods 2–3. The presence of CW or CCW loops and their interchanges on intraday timescales were reported by T09 from the XRT observations of our target in 2006 June.

5.5. The Position of Synchrotron SED Peak

Our spectral study of Mrk 421 has revealed a very wide range of the parameter E_p during 2013 November–2015 June. In lower X-ray states, the synchrotron SED peak was situated at energies as low as a few eV, while the source was a hard X-ray-peaking HBL on 10 occasions in this period. Note that the position of synchrotron SED peak for the PL spectra discussed in Section 4.2, derived via the fit of the corresponding broadband SED with the log-parabolic function (introduced by Landau et al. 1986)

$$\log \nu F_\nu = A(\log \nu)^2 + B(\log \nu) + C, \quad (5)$$

was not far beyond the XRT instrumental range, where it is difficult to evaluate a possible curvature, and the PL model gives a relatively better description of the spectrum (see Massaro et al. 2008). Therefore, a PL shape of these spectra should be rather related to the absence of the physical conditions in the emission zone producing a curved distribution of X-ray-emitting electrons with energy.

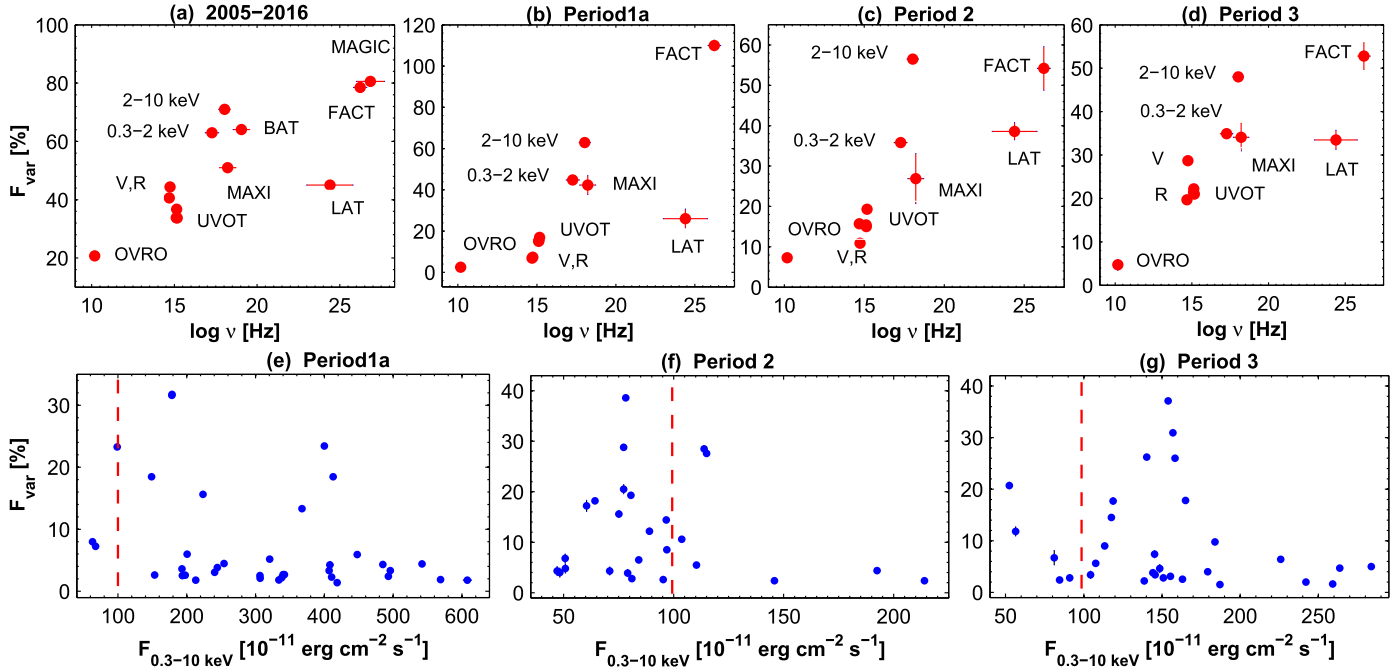

Figure 12. Top row: $F_{\rm var}$ as a function of the energy in different periods; bottom row: $F_{\rm var}$ of the 0.3–10 keV IDVs plotted vs. flux in different periods.

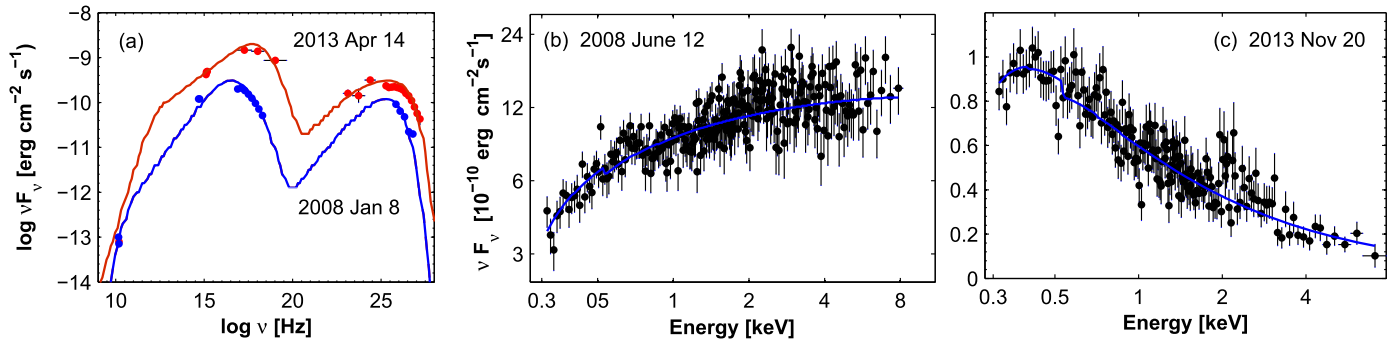

Figure 13. (a) Broadband SEDs, with red and blue curves representing a one-zone SSC fit to the observed spectral points (see Paper I for the model description). (b and c) 0.3–10 keV SEDs, with blue lines representing an LP fit of Mrk 421, corresponding to high and low brightness states.

In contrast to Period 1a, the position of the synchrotron SED peak did not shift beyond 10 keV in 2013 November–2015 June,[12] and Mrk 421 was a hard X-ray-peaking HBL 28 times in the former period. Therefore, the underlying physical conditions should be more extreme in our target during the 2013 April outburst, since the SED peak position is related to the jet physical parameters as $E_{\rm p} \propto \gamma_{3p}^2 B\delta$ (T09), where γ_{3p} is the peak of the distribution $n(\gamma)\gamma^3$; B is the magnetic field strength, and δ is the Doppler factor. Generally, the physical conditions in the jet of Mrk 421 should be highly variable from epoch to epoch, which is reflected in the SEDs obtained during different brightness states. Namely, Figure 13(a) presents the broadband SEDs obtained during the giant X-ray flares in 2013 April and those corresponding to the low X-ray/HVE states in 2008 January. Figure 13(b) shows the 0.3–10 keV SEDs corresponding to one of the highest historical X-ray states observed in 2008 June (MJD 54,630.3; extracted from the first 100 s segment of the fifth orbits of ObsID 30352099 and fitted with the LP model yielding $a = 1.72 \pm 0.02$, $b = 0.13 \pm 0.04$, $E_{\rm p} = 11.94 \pm 1.07$ keV, $F_{0.3-10\,\rm keV} = (3.70 \pm 0.07) \times 10^{-9}$ erg cm^{-2} s^{-1}), while that corresponding to a low X-ray state in the start of Period 2 is provided in Figure 13(c) (extracted from ObsID 31202141; see Table 4 for the fit results).

Moreover, the detection of the correlation $S_{\rm p} \propto E_{\rm p}^{\alpha}$ can be used to draw a conclusion about the physical factor that makes the main contribution to the observed spectral variability of the source, depending on the values of the exponent α (see Massaro et al. 2008; T09). However, we have not detected this correlation at the 99% confidence level either for any period or for particular subperiods (similar to Period 1a). The only exclusion was the second epoch of the second X-ray flare in Period 3c (with a peak on MJD 56,110; Figure 3(g)), which shows a weak positive $S_{\rm p}$–$E_{\rm p}$ correlation. However, the value of the exponent $\alpha = 0.29 \pm 0.14$ is beyond the range corresponding to the well-studied cases (see Tramacere et al. 2011): from $\alpha = 0.6$ to $\alpha = 4$ (in the former case, the momentum-diffusion coefficient and the exponent describing the turbulence spectrum are variable during the stochastic acceleration process of the particles, while the main driver is a variability of δ in the latter case). Therefore, we conclude that the physical conditions

[12] Equation (5) shows the position of synchrotron SED peak at energies $E < 10$ keV for the hardest PL spectra.

underlying the spectral variability of Mrk 421 during 2013–2015 were of a complex character, and the observed spectral changes could not be defined by a single factor.

5.6. Photon Index

The source also underwent an extreme spectral variability in the 0.3–10 keV band and exhibited an evolution from the softest spectrum with the photon index at 1 keV $a = 2.69 \pm 0.02$ in a quiescent state to the hardest value with $a = 1.75 \pm 0.02$ during one of the X-ray flares observed in Period 3. However, the source showed a more extreme variability during 2013 January–May with $a = 1.68$–2.83 and varied faster on intraday timescales (e.g., a hardening by $\Delta a = 0.12$ in 470 s and a softening by $\Delta a = 0.10$ were recorded during the giant outburst; Paper I). From the previous X-ray spectral studies of Mrk 421, even harder spectra with $a = 1.63$–1.67 were reported by T09 from the XRT observations performed during 2006 April–July, and 87% of the spectra from this period showed $a < 2$. During the 2008 June flare, the source was as hard as $a = 1.65$ (Donnarumma et al. 2009). The hardest spectra with $a = 1.34$–1.45 were reported by Ravasio et al. (2004) from the two *XMM-Newton* observations in 2002 November–December, and the LP fit yielding $a = 1.16$–1.50 for another two spectra was not satisfactory. Therefore, these values of the photon index cannot be credible. The *BeppoSAX* observations of 1997–2000 showed a wide range $a = 1.70$–2.54 (M04).

In the period presented here, the source also showed PL spectra, although their percentage was smaller than in 2013 January–May (5% of all 0.3–10 keV spectra vs. 13% in the latter period), and the 0.3–10 keV photon index showed a wider range $\Gamma = 1.70$–2.76, with a larger and faster variability on intraday timescales.

Although T09 presented the results of the LP fit with all the spectra from the 2006 April–July epoch, we have checked that for most of these spectra with $b < 0.09$ the LP fit does not give a better statistic than the PL fit. PL spectra with $\Gamma = 1.52$–1.60 in the 0.6–10 keV band were reported by Ravasio et al. (2004), and spectra with $\Gamma = 1.97$–2.90 in the 4–15 keV band were reported by Rebillot et al. (2006).

Our target showed the spectra harder than $a = 1.6$ significantly rarely in Mrk 501 (during the prolonged X-ray flaring activity in 2014 March–October; Kapanadze et al. 2017a) and 1ES 1959+650 (during 2015 August—2016 August; Kapanadze et al. 2016a, 2017b). Note that Mrk 421 sometimes exhibited very hard 0.3–300 GeV spectra during 2013 November–2015 June with $\Gamma < 1.70$ down to $\Gamma = 1.37 \pm 0.14$ from the 1-week binned LAT data. According to Shukla et al. (2015), the origin of a very hard γ-ray spectrum can be obtained much more easily within hadronic scenarios, whereas achieving a hard spectrum from leptonic models is more demanding. Note that such very hard spectra were shown by the source during MJD 57,029–57,043, MJD 57,058–57,065, and MJD 57,085–57,092 when an uncorrelated X-ray–HE/VHE variability was observed, to be explained more easily in the framework of hadronic scenarios.

6. Conclusions

We have presented the results of X-ray observations of the HBL source Mrk 421 performed with *Swift*-XRT during 2013 November–2015 June. It exhibited a strong long-term variability of the 0.3–10 keV flux with the maximum-to-minimum ratio of 13. On weekly timescales, the source showed X-ray flares by a factor of 1.8–5.2, and the 0.3–10 keV count rate almost attained 100 counts s^{-1} in Period 3 (corresponding to 3.1×10^{-9} erg cm^{-2} s^{-1}). We detected 48 XRT instances of 0.3–10 keV IDVs, which mostly occurred in high X-ray states in Period 3. They were characterized by fractional variability amplitudes of 1.5(0.3)%–38.6(0.4)%, and the source showed unequal activity on intraday timescales in different epochs: it sometimes varied within the 1 ks observational runs (nine instances), while the flux changed very slowly during some densely sampled XRT observations. The largest IDVs incorporated a flux doubling in 20.4 hr and a decline by a factor of 2.2 in 3.1 hr. For the whole period, the fractional variability amplitude showed a double-humped shape with the highest variability in the X-ray and VHE bands. The XRT and FACT observations often showed a correlated variability, although we found some occasions that pose a challenge to one-zone SSC scenarios: a strong TeV flare was not accompanied by comparable X-ray activity and vice versa. The LAT-band and optical–UV fluxes mostly exhibited an uncorrelated variability with the X-ray one, while there was a positive correlation between the 0.3–300 GeV and UVOT-band fluxes (expected in the case of the KN suppression in the IC process, yielding an effective upscatter of optical–UV photons to GeV energies by the electrons, radiating in X-rays).

Along with a strong flux variability, the source also showed an extreme spectral behavior. A total of 95% of the spectra were curved, and the position of the SED peak underwent an overall variability by more than 3.2 orders in frequency, from a few eV to 9.15 ± 0.94 keV. The source mostly showed a relatively small X-ray spectral curvature and an anticorrelation with the position of the SED peak, expected in the case of effective stochastic acceleration of X-ray-emitting electrons. During the X-ray flare in Period 3b, the curvature parameter showed a positive correlation with the photon index that is expected in the framework of the EDAP scenario. The photon index at 1 keV and HR exhibited wide ranges ($a = 1.75$–2.69 and HR = 0.22–1.14) and a strong variability on diverse timescales. During X-ray flares, the source mainly exhibited a "harder-when-brighter" spectral evolution, and the strength of this trend varied significantly among the subperiods of Period 2. In the HR—flux plane, the spectral evolution mostly followed CW-type loops in Period 3 (consistent with the dominance of synchrotron cooling), while the source showed a more complex interplay between the electron acceleration, synchrotron cooling, and flux variability timescales (a change to the opposite trend even during the particular flare) in the previous period.

We conclude that Mrk 421 is one of the most extreme HBLs with a very complex, unpredictable timing/spectral variability, exclusively strong X-ray flares in some epochs, and X-ray/HE/VHE flares often challenging a one-zone SSC scenario. Further intensive, satellite and ground-based MWL campaigns will be very useful for gaining a proper understanding of high-energy processes in relativistic jets and the innermost AGN area.

B.K., S.K., and L.T. acknowledge the Shota Rustaveli National Science Foundation and Ilia State University for research grant FR/377/6-290/14. P.R. acknowledges contract

ASI-INAF I/004/11/0. D.D. acknowledges funding by the German BMBF (Verbundforschung Astro- und Astroteilchenphysik) and HAP (Helmholtz Alliance for Astro-particle Physics). We thank the FACT Collaboration for making their analysis results publicly available, and we appreciate very much their long-term monitoring initiative, which provides precious input for MWL studies. This research has made use of the XRTDAS software, developed under the responsibility of the ASDC, Italy, and the data from the OVRO 40 m monitoring program, which is supported in part by NASA grants NNX08AW31G and NNX11A043G and NSF grants AST-0808050 and AST-1109911. This research has made use of the VizieR catalog access tool, CDS, Strasbourg, France. The original description of the VizieR service was published in *A&AS*, 143, 23. We acknowledge the use of the VHE data from long-term Whipple observations, published in *Aph*, 51, 1. We thank the anonymous referee for his/her very useful comments and suggestions that helped to improve the quality of the paper.

ORCID iDs

B. Kapanadze https://orcid.org/0000-0002-7146-6751
P. Romano https://orcid.org/0000-0003-0258-7469
S. Vercellone https://orcid.org/0000-0003-1163-1396

References

Acciari, V. A., Aliu, E., Arlen, T., et al. 2011, ApJ, 738, 25
Acciari, V. A., Arlen, T., Aune, T., et al. 2014, Aph, 54, 1
Acero, F., Ackermann, M., Ajello, M., et al. 2015, ApJS, 218, 23
Ahnen, M. L., Ansoldi, S., Antonelli, L. A., et al. 2016, A&A, 593, 91
Albert, J., Aliu, E., Anderhub, H., et al. 2008, ApJ, 674, 1037
Alecsic, J., Ansoldi, S., Antonelli, L. A., et al. 2015a, A&A, 576, 126
Alecsic, J., Ansoldi, S., Antonelli, L. A., et al. 2015b, A&A, 578, 22
Anderhub, H., Backes, M., Biland, A., et al. 2013, JInst, 8, P06008
Andruchow, I., Romero, G. E., & Cellone, S. A. 2005, A&A, 442, 57
Atwood, W. B., Abdo, A. A., Ackermann, M., et al. 2009, ApJ, 697, 1071
Balocovic, M., Paneque, D., Madejski, G., et al. 2016, ApJ, 819, 156
Barthelmy, S. D., Barbier, L. M., Cummings, J. R., et al. 2005, SSRv, 120, 143
Bessel, M. S. 1979, PASP, 91, 589
Blazejowski, M., Blaylock, G., Bond, I. H., et al. 2005, ApJ, 630, 130
Breeveld, A. A., Landsman, W., Holland, S. T., et al. 2011, in AIP Conf. Ser. 1358, Gamma Ray Bursts (Melville, NY: AIP), 373
Burrows, D. N., Hill, J. E., Nousek, J. A., et al. 2005, SSRv, 120, 165
Celotti, A., & Ghisellini, G. 2008, MNRAS, 385, 283
Cui, W. 2004, ApJ, 605, 662
Donnarumma, I., Vittorini, V., Vercellone, S., et al. 2009, ApJL, 691, L13
Dorner, D., Ahnen, M. L., Bergmann, M., et al. 2015, arXiv:1502.02582
Falcone, A. D., Cui, W., & Finley, J. P. 2004, ApJ, 601, 165
Falomo, R., Pian, E., & Treves, A. 2014, A&ARv, 22, 73
Fitzpartick, E. L., & Messa, D. 2007, ApJ, 663, 320
Fukugita, M., Shimasaku, K., & Ichikawa, T. 1995, PASP, 107, 945
Furniss, A., Noda, K., Boggs, S., et al. 2015, ApJ, 812, 65
Gehrels, N., Chincarini, G, Giommi, P., et al. 2004, ApJ, 611, 1005
Horan, D., Acciari, V. A., Bradbury, S. M., et al. 2009, ApJ, 695, 596
Kalberla, P. M. W., Burton, W. B., Hartmann, D., et al. 2005, A&A, 440, 775
Kapanadze, B., Dorner, D., Romano, P., et al. 2017a, MNRAS, 869, 1655
Kapanadze, B., Dorner, D., Vercellone, S., et al. 2016a, ApJ, 831, 102
Kapanadze, B., Dorner, D., Vercellone, S., et al. 2017b, MNRAS, in press https://doi.org/10.1093/mnras/stx2492
Kapanadze, B., Romano, P., Vercellone, S., et al. 2016b, MNRAS, 457, 704
Kapanadze, B., Romano, P., Vercellone, S., & Kapanadze, S. 2014, MNRAS, 444, 1077
Krimm, H., Holland, S. T., Corbet, R. H. D., et al. 2013, ApJ, 209, 14
Landau, R., Golisch, B., Jones, T. J., et al. 1986, ApJ, 308, 78
Mangalam, A. V., & Wiita, P. J. 1993, ApJ, 406, 420
Mannheim, K., & Biermann, P. L. 1992, A&A, 253, L21
Marscher, A. P., & Gear, W. K. 1985, ApJ, 298, 114
Massaro, E., Perri, M., Giommi, P., & Nesci, R. 2004, A&A, 413, 489
Massaro, F., Paggi, A., & Cavaliere, A. 2011, ApJL, 742, L32
Massaro, F., Tramacere, A., Perri, M., Giommi, P., & Tosti, G. 2008, A&A, 448, 861
Matsuoka, M., Kawasaki, K., Ueno, S., et al. 2009, PASJ, 61, 999
Max-Moerbeck, W., Richards, J. L., Hovatta, T., et al. 2014, MNRAS, 445, 437
Nilsson, K., Pasanen, M., Takalo, L. O., et al. 2007, A&A, 475, 199
Padovani, P., & Giommi, P. 1995, ApJ, 444, 567
Page, M., Kuin, N. P. M., Breeveld, A. A., et al. 2013, MNRAS, 436, 1684
Poole, T. S. 2008, MNRAS, 383, 627
Preziuso, S. 2013, PhD thesis, Univ. Pisa
Ravasio, M., Tagliaferri, G., Ghisellini, G., & Tavecchio, F. 2004, A&A, 424, 841
Rebillot, P. F., Badran, H. M., & Blaylock, G. 2006, ApJ, 641, 740
Richards, J. L., Max-Moerbeck, W., Pavlidou, V., et al. 2011, ApJS, 194, 209
Romano, P., Campana, S., Chincarini, G., et al. 2006, A&A, 456, 917
Romero, G. E., Cellone, S. A., & Combi, J. A. 1999, A&AS, 135, 477
Roming, P. W. A., Kennedy, T. E., Mason, K. O., et al. 2005, SSRv, 120, 95
Saito, S., Stawarz, Ł., Tanaka, Y. T., et al. 2013, ApJL, 766, L11
Shukla, A., Chitnis, V. R., Singh, B. B., et al. 2015, ApJ, 798, 2
Sinha, A., Shukla, A., Saha, L., et al. 2016, A&A, 591, 83
Smith, P. S., Montiel, E., Rightley, S., et al. 2009, arXiv:0912.3621
Sokolov, A., Marscher, A. P., & McHardy, I. M. 2004, ApJ, 613, 725
Steinke, B. 2012, PhD thesis, Tech. Univ. Munich
Takahashi, T., Kataoka, J., Madejski, G., et al. 1996, ApJL, 470, L89
Tramacere, A., Giommi, P., Perri, M., Verrecchia, F., & Tosti, G. 2009, A&A, 501, 879
Tramacere, A., Massaro, E., & Taylor, A. 2011, ApJ, 739, 66
Urry, C. M., & Padovani, P. 1995, PASP, 107, 803
Vaughan, S., Edelson, R., Warwick, R. S., & Uttley, P. 2003, MNRAS, 345, 1271